JCI The Journal of Clinical Investigation

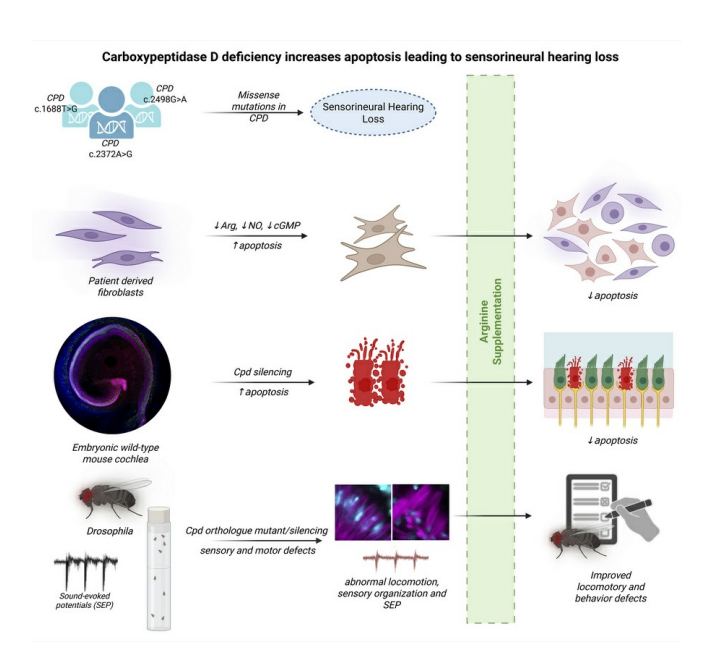
Carboxypeptidase D deficiency causes hearing loss amenable to treatment

Memoona Ramzan, ..., R. Grace Zhai, Mustafa Tekin

J Clin Invest. 2025. https://doi.org/10.1172/JCI192090.

Research In-Press Preview Genetics Otology

Graphical abstract



Find the latest version:



Carboxypeptidase D deficiency causes hearing loss amenable to treatment

Memoona Ramzan^{1*}, Natalie Ortiz-Vega^{2,3*}, Mohammad Faraz Zafeer^{1*}, Amanda G. Lobato^{2,3*}, Tahir Atik⁴, Clemer Abad¹, Nirmal Vadgama⁵, Duygu Duman^{6,7}, Nazım Bozan⁸, Enise Avcı Durmuşalioğlu⁴, Sunny Greene², Shengru Guo¹, Suna Tokgöz-Yılmaz⁶, Merve Koç Yekedüz^{9,10}, Fatma Tuba Eminoğlu^{7,9}, Mehmet Aydın⁸, Serhat Seyhan¹¹, Ioannis Karakikes⁵, Vladimir Camarena¹, Maria Camila Robayo¹, Tijana Canic³, Güney Bademci¹², Gaofeng Wang^{1,12}, Amjad Farooq¹³, Mei-ling A Joiner¹⁴, Katherina Walz^{1,12,15}, Daniel F Eberl¹⁴, Jamal Nasir¹⁶, R. Grace Zhai^{2,3#}, Mustafa Tekin^{1,12#}

¹John P. Hussman Institute for Human Genomics, University of Miami Miller School of Medicine, Miami, FL, USA

²Department of Molecular and Cellular Pharmacology, University of Miami Miller School of Medicine, Miami, FL, USA

³Department of Neurology, University of Chicago, Chicago, IL, USA

⁴Division of Pediatric Genetics, Department of Pediatrics, School of Medicine, Ege University, Izmir, Türkiye

⁵Department of Cardiothoracic Surgery, Stanford University, Stanford, CA, USA

⁶Department of Audiology, Ankara University Faculty of Health Sciences, Ankara, Türkiye

⁷Ankara University Rare Diseases Application and Research Center, Ankara, Türkiye

⁸Department of Otolaryngology, Faculty of Medicine, Yüzüncü Yıl University, Van, Türkiye

⁹Division of Pediatric Metabolic Diseases, Department of Pediatrics, Ankara University School of Medicine, Ankara, Türkiye

¹⁰Harvard Medical School, Boston Children's Hospital, Department of Anesthesiology, Critical Care and Pain Medicine, Boston, MA, USA ¹¹Laboratory of Genetics, Memorial Şişli Hospital, Istanbul, Türkiye

¹²Dr. John T. Macdonald Foundation Department of Human Genetics, University of Miami Miller

School of Medicine, Miami, FL, USA

¹³Department of Biochemistry, University of Miami Miller School of Medicine, Miami, FL, USA

¹⁴University of Iowa, Iowa City, USA

¹⁵Instituto de Química Biológica de la Facultad de Ciencias Exactas y Naturales (IQUIBICEN)

CONICET, Argentina

¹⁶Division of Life Sciences, University of Northampton, UK

*These authors contributed equally

***Correspondence to:**

Mustafa Tekin

1501 NW 10th Avenue, BRB-610 (M860)

Miami, FL 33136

Phone: +1 (305)243-2381

E-mail: mtekin@med.miami.edu

Or

R. Grace Zhai

5812 South Ellis Avenue

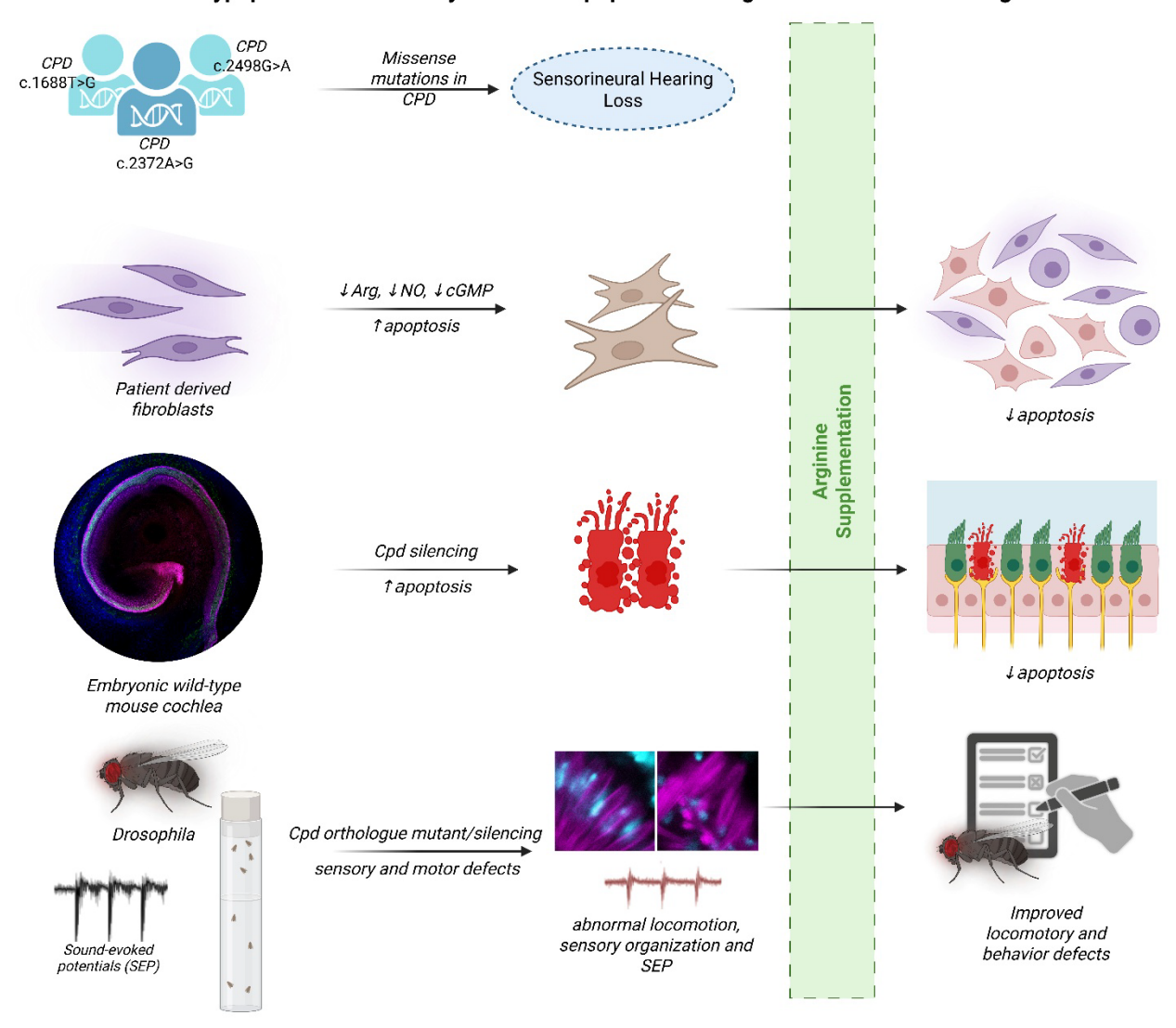
MC 2030, SBRI J310

Chicago, IL 60637

Phone: +1 773-702-6390

E-mail: rgzhai@uchicago.edu

Carboxypeptidase D deficiency increases apoptosis leading to sensorineural hearing loss



Abstract

Genetic factors contributing to hearing loss (HL) are heterogeneous, and effective medical treatments remain limited. We identified three distinct missense variants in CPD, encoding carboxypeptidase D, in five individuals with congenital deafness from three unrelated families, affecting the catalytically active CP-domain2 of this protein. Subsequent analysis of a larger cohort from the 100,000 Genomes Project (100KGP), revealed an enrichment of rare protein-altering CPD variants in individuals with HL. We show that CPD localizes to sensory epithelium and nerve cells in the mouse cochlea, and the enzymatic activity of CPD, crucial for nitric oxide (NO) production through arginine processing, is impaired in affected individuals. The levels of arginine, NO, and cyclic guanosine monophosphate (cGMP) in patient-derived fibroblasts are also decreased, leading to increased oxidative stress and cell death via endoplasmic reticulum stressmediated mechanisms. Silencing of Cpd in organotypic mouse cochlea cultures leads to increased apoptosis. Finally, Drosophila models of CPD deficiency display defective Johnston's organ, impaired auditory transduction, and sensory and movement abnormalities. Notably, these phenotypes are partially rescued by the supplementation with arginine or sildenafil, a cGMP enhancer. Our findings establish CPD mutations as a cause of congenital HL, highlighting that the NO signaling pathway offers a promising therapeutic avenue.

Keywords: arginine, cGMP, CPD deficiency, hearing loss, nitric oxide, unfolded protein response

INTRODUCTION

Hearing loss (HL) affects approximately 1 in 500 newborns and becomes increasingly common with age, impacting nearly half of adults over 65 years old (1, 2). It often results from dysfunction in the delicate structures or complex signaling pathways of the cochlea (3). Among the recognized auditory pathways, the role of nitric oxide (NO) signaling is not thoroughly characterized. Conventionally, NO is synthesized from arginine and oxygen in the presence of NO synthase (NOS) and cofactors (4). The arginine used as a substrate to produce NO can be generated by metallocarboxypeptidases, a group of zinc-dependent enzymes involved in the catalytic cleavage of proteins at the carboxyl terminus (5). Carboxypeptidase D (CPD) is an important member of this enzyme family and possesses the ability to cleave peptides with the C-terminal arginine or lysine (5).

Previous studies have shown that NO signaling is involved in sensory hair cells, supporting cells, and spiral ganglion in the cochlea (6-10), as well as in the brainstem, where the cochlear nucleus is located (11-15). Perturbation of NO signaling has been implicated in endoplasmic reticulum (ER) stress and mitochondrial dysfunction across various diseases (16-18). However, the integrated role of NO in hearing remains poorly understood, and no hereditary form of deafness has been directly linked to mutations in components of the NO signaling pathway.

Sensorineural hearing loss (SNHL) is the most common type of permanent HL, caused by damage to the cochlea or the auditory nerve (19). SNHL is generally irreversible, and although hearing aids and cochlear implants are commonly used to improve hearing, they do not completely restore physiological functioning. Recently, the first gene therapy clinical trials for hereditary deafness have shown promising results (20). However, medical treatment for hereditary deafness is not readily available.

Our study identifies CPD as a critical regulator of metabolic signaling, linking arginine and NO to cochlear cell survival. We describe three unrelated families with *CPD* variants identified via genome sequencing (GS) and exome sequencing (ES). Our *in vitro* and *in vivo* functional analyses show that dysfunction of *CPD* causes NO deficiency and apoptosis, which can potentially be treated using dietary supplements rich in arginine.

RESULTS

CPD variants in three families with deafness

The families reported here are a part of an international cohort comprising 1,012 families with SNHL. Among these, 441 families remained unsolved after excluding single nucleotide variants (SNVs), small insertions and deletions (indels), and copy number variants (CNVs) in all known deafness genes via ES and GS. Affected individuals in three Turkish families presented in this study have congenital or prelingual-onset, bilateral severe-profound or profound SNHL (Figure 1A, Supplementary Figure 1). The detailed systemic physical examinations in the affected individuals show no other clinical findings associated with HL, and gross vestibular function is normal (Table 1, Supplementary Table 1, 2).

As detailed in the methods, we analyzed ES and GS data, focusing on rare variants co-segregating with HL in each family. The proband of family 1 is homozygous for a missense variant, c.1688T>G; p.(Met563Arg) in *CPD* mapping to an autozygous region on chromosome 17 and co-segregating with HL within the extended family (Figure 1A, Supplementary Figure 2A, and Table 1, Supplementary Table 1). Further analysis via GS did not reveal any plausible coding/non-coding variants or CNVs in recognized genes for deafness. Specifically, no pathogenic variants were identified in *MYO15A* or *GRAP*, which map to the same chromosomal region. In the probands of

families 2 and 3, we identified the missense variants c.2498G>A p.(Arg833His) and c.2372A>G p.(Gln791Arg) in *CPD*, respectively. Both variants co-segregate with HL in an autosomal recessive pattern (Figure 1A, Supplementary Figure 2A, and Table 1, Supplementary Table 1).

Functional CPD variants are enriched in HL probands as compared to controls

To assess the broader impact of *CPD* variants at the population level and investigate whether they might contribute to HL later in life, we conducted a burden analysis using a large cohort from the 100,000 Genomes Project (100KGP) (21). It comprised of 3,802 individuals with HL and 27,503 controls. This allowed us to determine the extent to which rare protein-altering variants influence disease susceptibility beyond the severe cases identified in family studies.

Due to Genomics England policy, individual-level clinical data from the 100KGP cannot be disclosed, and only aggregate summaries of phenotypic information are permitted. Nevertheless, most cases with rare *CPD* variants exhibited features highly consistent with the clinical profile observed in our familial cases, including congenital or childhood-onset bilateral SNHL, with severity ranging from severe-profound. Several individuals also underwent MRI imaging of the internal auditory meatus, with findings consistent with primary inner ear dysfunction, in keeping with the expected cochlear and neuronal localization of *CPD*.

A subset of individuals displayed additional or potentially unrelated features, including middle ear pathologies such as otitis media or conductive HL. While these findings may suggest comorbid or acquired conditions rather than the primary consequence of *CPD* dysfunction, we retained these individuals in the broader analysis to avoid overly restrictive filtering that might obscure the contribution of *CPD* variants to a genetically heterogeneous clinical spectrum.

The analysis of all protein-altering variants in CPD showed an alternate allele frequency of 2.69% in cases and 2.19% in controls, yielding an odds ratio (OR) of 1.23 (95% CI: 1.06–1.44, p = 0.0084). This result indicates a statistically significant but modest enrichment of protein-altering variants in cases compared to controls (Figure 1B, Supplementary data).

For prioritized missense variants with a minor allele frequency (MAF) < 0.001 and either a CADD score ≥ 25 or an AlphaMissense score indicating probable damage or ambiguity (≥ 0.34), the alternate allele frequency was 0.26% in cases and 0.15% in controls, resulting in an OR of 1.81 (95% CI: 1.11–2.96, p=0.0211). This suggests a statistically significant association, with prioritized missense variants being more frequent in cases. Furthermore, analysis of loss-of-function (LoF) variants revealed an alternate allele frequency of 0.07% in cases and 0.02% in controls. The OR was 3.02 (95% CI: 1.06–8.57, p=0.0465), demonstrating a significant enrichment of LoF variants in cases (Figure 1B, Supplementary data). This category exhibited the strongest association among all variant groups.

The combined category of prioritized missense and LoF variants showed an alternate allele frequency of 0.33% in cases and 0.17% in controls. The OR was 1.97 (95% CI: 1.27–3.07, p = 0.0042), reflecting a statistically significant association, with these variants being more frequent in cases (Figure 1B).

In silico modeling predicts reduced catalytic activity in CPD mutants

CPD consists of three CP-domains, extracellular N-terminal, cytosolic C-terminal, and a small transmembrane domain (Supplementary Figure 2B). All detected variants affect highly conserved amino acids localized in the catalytically active CP-domain 2 (Supplementary Figure 2B).

CP-domain 2 is comprised of an N-terminal $\alpha\beta$ -fold harboring a Zn^{2+} divalent ion as a cofactor at the active site and a C-terminal β -barrel (Figure 1D). Met563 forms a part of a group of residues that give structural integrity to the catalytic center of the protein (Figure 1D). The p.Met563Arg variant would lead to distortion of the active site due to the bulky, basic side chain of arginine (Figure 1D). Moreover, it would also serve as a non-competitive inhibitor of potential substrates.

The sidechain moiety of Gln791 is not only exposed to the solvent but, along with other polar residues, it enables the protein to "breathe," thereby enforcing rapid substrate turnover. The substitution of Gln791 with arginine leads to the formation of an additional salt bridge with the neighboring Glu710 (Figure 1E). The resulting molecular interaction causes structural disruption and forms an additional layer of rigidity to the protein, compromising its catalytic activity.

Arg833 forms a salt bridge with Asp696 (Figure 1E), which tethers the β -barrel to the back of the $\alpha\beta$ -fold, away from its catalytic center, and is critical for overall structural integrity. The p.Arg833His variant would destabilize the protein and likely deactivate it by distorting its catalytic center (Figure 1D).

CPD localization in mouse cochlea and antibody validation

We detected *Cpd* mRNA expression in the cochlea of embryonic (E18.5), neonatal (P0), and adult mice (P15 and P30) via quantitative and semi-quantitative RT-PCR analysis. *Cpd* is consistently expressed across cochlear development and is present in multiple cochlear cell types (Supplementary Figure 3A, B). Immunostaining with validated anti-CPD antibody (Supplementary Figure 4, Supplementary Figure 5) on cochlear sections from wild-type mice shows localization of CPD in both inner and outer hair cells, stria vascularis, and spiral ganglion (Figure 1C, Supplementary Figure 4). This pattern is consistent mainly with public RNA-seq and

single-cell RNA-seq (scRNA-seq) datasets available via the gEAR portal (https://umgear.org), which show strong expression in the hair cells, stria vascularis and spiral ganglion (Supplementary Figure 3C, D). Together, these complementary data highlight the broad and sustained presence of CPD in the cochlea, supporting its relevance throughout development and into postnatal maturation.

Reduced enzyme activity and altered protein length in CPD mutants

CPD is known to cleave the C-terminal Arg/Lys of its substrates. Thus, the disruption in the catalytic domain of the enzyme is expected to decrease the efficiency of peptide cleavage, resulting in longer peptides or unused substrate. It is evident in Figure 2A that when the lysate containing the mutated CPD was incubated with dansyl-Ala-Arg, a significant amount of the substrate was left uncleaved. This is supported by LC/MS data analysis, which reveals a relative increase in longer peptides from patients' fibroblasts compared to the control group (Figure 2B).

Low levels of Lysine, Arginine, NO, and cGMP in patient fibroblasts rectified by exogenous Arginine

The cleaved arginine by CPD could serve as a substrate for NOS to produce NO, which in turn signals various biological processes, including the conversion of GTP to cGMP (22). To test this, we first measured the levels of intracellular arginine (and lysine) in control and patient fibroblasts. We observed a decrease in both amino acids in patient cells compared to control (Figure 2C, Supplementary Figure 6A). Further, NO and cGMP levels were also reduced in patient cells when compared to the control group (Figures 2D, E, Supplementary Figure 6B, C). These results support the hypothesis that the disruption of the catalytic site of CPD leads to a reduction of intracellular arginine, lysine, and NO signaling.

We subsequently administered L-Arginine to patient fibroblasts, which reversed the levels of intracellular NO and cGMP to almost normal levels, compared to the control groups (Figures 2D, E, Supplementary Figure 6B, C). These results suggest that the identified variants cause damage to the catalytic domain of CPD, reduction of intracellular arginine, and defective NO signaling, which can be reversed with the supplementation of arginine.

Decrease in NO levels causes apoptosis in fibroblasts

NO plays a protective role in cells by triggering the activation of different kinases in canonical pathways (23). These include ERK activation, CREB and AKT, which have notable consequences on neuronal development and survival (23). Intending to identify the impact of decreased NO levels on fibroblasts, we cultured patient and control fibroblasts. We analyzed the DNA fragmentation as well as phosphorylation of AKT, ERK, CREB, and BAD proteins through Western blotting. Terminal deoxynucleotidyl transferase dUTP nick end labeling (TUNEL) assay revealed that fibroblasts with CPD mutations have a larger proportion of cells undergoing apoptosis (Figure 3A, Supplementary Figure 6D). In addition, the patients' fibroblasts have significantly higher proportions of apoptosis markers AnnexinV and propidium iodide (PI) positive cells as compared to controls (Figure 3B and C, Supplementary Figure 6E). However, when patients' cells were supplemented with arginine, there was a reduction in apoptosis (p < 0.05) among these cells (Figure 3C, Supplementary Figure 6E, Supplementary Figure 7). Since lysine is also an essential amino acid and is known for its role in cell growth and survival processes, we also tested the effect of lysine in reducing apoptosis in patient fibroblasts; results suggest that it was much less effective or ineffective when administered alone or in combination with arginine (Supplementary Figure 7). Lysine and arginine may interact negatively as they compete for the same transporter (CAT) to enter the same cell. Arginine is well known for its role in metabolic

stress adaptation by different cells (24), and lysine is mainly involved in protein and collagen synthesis, and histone modifications (25).

We were unable to identify a significant change in canonical apoptotic protein levels (AKT/pAKT, CREB/pCREB, BAD/pBAD, and caspases) in patient fibroblasts compared to controls (Supplementary Figure 8A-D). This led us to investigate alternative apoptotic pathways. As mentioned earlier, NO deficiency can have an impact on oxidative stress, mitochondrial dysfunction, ER stress, and/or p53 activation related to apoptosis (17, 18). We, therefore, tested fibroblasts for oxidative stress by measuring the relative fluorescence intensity of cells after loading with 2',7'-dichlorodihydrofluorescein diacetate (H₂DCFDA). The patients' cells showed significantly increased oxidative stress (Figure 3D, Supplementary Figure 6F) and lower ratios of red/green fluorescence intensity, indicating compromised mitochondrial function (Figure 3E, Supplementary Figure 6G). Oxidative stress and mitochondrial dysfunction are expected to lead to ER stress and p53 activation. As shown in Figures 3F, G, and Supplementary Figure 6H-I, spliced XBP1 (sXBP1) and CHOP, markers of ER stress/unfolded protein response (UPR), as well as p53 levels for oxidative stress, are increased in patients' fibroblasts.

Silencing of *Cpd* leads to apoptosis in murine cochlear cells

Since Cpd expression was localized in the inner ear, we analyzed the effect of silencing Cpd in mouse cochlear explants. The expression of Cpd was reduced in cochlea transfected with scrambled (control) and Cpd siRNA lentiviruses at a multiplicity of infection (MOI) of 2×10^6 , compared to controls (Supplementary Figure 9). We analyzed TUNEL staining signals across apical, mid, and basal regions of the cochlea. Images were acquired at 63x using an oil immersion lens, and apoptotic cells were counted using ImageJ. The apoptosis was more intense in Cpd silenced explants when compared to controls (p < 0.001), indicating sensory cells in the cochlea

are undergoing apoptosis due to reduction in *Cpd* expression (Figure 4A, C). The supplementation of arginine for 24 hours was effective in reducing the apoptosis in the sensory epithelium of the cochlea (Figure 4B, C). These results suggest that the timely administration of arginine may be beneficial in treating loss of sensory epithelium in the cochlea.

Loss of silver impairs auditory processing and disrupts scolopidia organization

The *Drosophila* ortholog of CPD, encoded by the *silver* gene (*svr*), is highly conserved and serves as a robust model for CPD dysfunction with a DIOPT (Drosophila RNAi Screening Center Integrative Ortholog Prediction Tool) score of 12/16 (26). The silver gene is alternatively spliced to produce long transmembrane forms with 3 CP-like domains and short soluble forms with a single CP domain (27). Recent studies have highlighted the molecular and genetic conservation of the mechanosensory transduction in flies and vertebrates (28-30). Analysis of single-cell RNA-Seq of the adult *Drosophila* antenna obtained from Fly Cell Atlas (FCA) (31) with Scope visualization confirms that *svr* is highly expressed in the antenna, including Johnston's organ (JO); the *Drosophila* hearing organ (Figure 5A-B). JO is the component of the auditory system required for sensing gravity, wind flow, and near-field sound (32).

Distinct classes of *svr* mutants have been described. Global loss of function alleles that reduce all CPD isoforms results in embryonic or larval lethality. In contrast, mutants specifically affecting long forms, such as *svr*¹ mutant (a 3bp deletion in exon 6, causing loss of a conserved leucine residue in the second CP-like domain and consequent loss of enzyme activity and protein misfolding), reduce the abundance of the long form and the activity of CPD (27). To further model CPD loss, we performed pan-neuronal knockdown (RNAi) of *svr* using *elav-GAL4*, which is significantly expressed in the antenna, including the JO neurons (Figure 5B).

JO contains approximately 200 scolopidia (Figure 5A), the fundamental mechanosensory units of hearing analogous to vertebrate hair cells (33). To assess the effect of loss of function of *svr* on JO, we assessed morphology of scolopidia using phalloidin staining. Both *svr*¹ mutants and panneuronal *silver-RNAi* flies exhibited disorganized actin bundles in the JO when compared to their respective controls, indicating deterioration of auditory organ structure (Figure 5C).

To assess whether loss of *svr* affects auditory function, we performed electrophysiology recordings of sound-evoked potentials (SEPs) from the antennal nerve. Control flies (*luciferase-RNAi*) exhibited robust SEP amplitudes, while *silver-RNAi* or *svr¹* mutants displayed an approximate 50% reduction in SEP amplitudes (Figure 5D, E), indicating significant impairment of auditory transduction. Collectively, these findings demonstrate that CPD deficiency caused by *svr* mutations or knockdown leads to both structural and functional impairment of the auditory system.

Loss of silver causes deficits in negative geotactic behavior in Drosophila

To determine whether *CPD* deficiency impacts broader JO-mediated behaviors, we assessed negative geotactic behavior, a sensitive measure of gravity sensing and motor coordination reliant on intact auditory/neurosensory circuits (26, 34). Therefore, while negative geotaxis isn't solely a measure of auditory processing, it relies on the function of the antenna and JO, which are critical for sound detection. Compared to wild-type *canton*-s (*cs*) controls, *svr*¹ shows significantly reduced speed (Figure 6A), movement direction (Figure 6B), and percentage of flies to reach a determined distance (7cm) in 10 seconds (Figure 6C). Additionally, longitudinal analysis of *silver-RNAi* revealed sustained deficits in speed and movement direction across ages (5, 10, and 25 days after eclosion [DAE]) in both females (Figures 6D, E) and males (Supplementary Figure 10 A, B), along with reduced percentage to reach 7cm in 10 seconds (Figure 6F). Lastly, we also measured the distance climbed in the first 5 seconds, and the kymograph showed a significant reduction in

climbing rate for *silver RNAi*-knockdown female (Figures 6G, H, J) and male flies when compared to control at 5, 10, and 25 DAE, respectively (Supplementary Figure 10 C, D, E). This suggests a delayed response in gravity sensing for the *silver-RNAi* flies when compared to the controls. Taken together, the results suggest that loss of *silver* by mutant deletion or pan-neuronal knockdown causes impaired negative geotactic behavior, and when combined with reduced auditory processing and impaired morphology, suggests impaired function of the *Drosophila* hearing organ.

Feeding with L-Arginine or Sildenafil improves negative geotactic behavior in *Drosophila* model of CPD deficiency

To test whether modulating the nitric oxide (NO) pathway could rescue deficits caused by CPD deficiency, we examined the effects of L-Arginine and sildenafil, a cGMP enhancer, in flies with pan-neuronal knockdown of *silver* by assessing the negative geotactic function of the flies after drug feeding at previously analyzed timepoints (Figure 7A). Both L-Arginine and sildenafil significantly improved the average speed for *silver-RNAi* at 5 DAE, and sildenafil continued to show improvement at 10 DAE (Figure 7B). Moreover, L-Arginine significantly improved movement direction at 5 and 10 DAE when compared to normal food, while sildenafil showed minor improvements (Figure 7C). Feeding with both drugs significantly improved distance climbed in the first 5 seconds at all timepoints, showing significant improvement of gravity sensing. (Figure 7D-F). Lastly, the percentage of flies that were able to reach 7cm in 10 seconds also improved with L-Arginine supplementation (Figure 7G-J). Unexpectedly, L-arginine or sildenafil feeding in control flies occasionally caused mild behavioral toxicity, evidenced by decreased performance (Supplementary Figure 11), suggesting context-dependent effects.

Overall, these findings demonstrate that loss of CPD/silver impairs the structure and function of the *Drosophila* auditory system and associated gravity-sensing behaviors, but that these deficits

can be partially ameliorated by pharmacological modulation of the NO-cGMP pathway. This suggests the beneficial effects of modulating NO pathways in enhancing the integrity and output of sensory-motor neurocircuitry in the context of CPD loss of function and highlights the translational potential of targeting this signaling cascade in conditions of CPD-deficient hearing loss.

DISCUSSION

CPD belongs to a family of metallocarboxypeptidases, which perform diverse physiological functions, ranging from the digestion of food to the biosynthesis of neuropeptides (35). It is a single-transmembrane protein harboring three catalytic carboxypeptidase domains, each of which requires a Zn^{2+} divalent ion as a cofactor (36, 37).

CPD's role in human health has been suggested in a few studies related to lupus erythematosus (38) and cancer (39); however, a hereditary disorder caused by CPD dysfunction has not been reported until this study. There are several known mutations for *CPD* in the ortholog of *Drosophila* that are collectively known as the *silver*, or *svr*, mutants. Along with the viable *svr* mutants there are many mutants reported to be embryonic lethal in the literature (38). Moreover, *Cpd* knockout mice do not survive (https://www.mousephenotype.org/). It is possible that complete loss of CPD function is not compatible with life in humans. In our study, we report missense *CPD* variants exclusively located within the CP-domain 2 that are predicted to disturb the catalytic activity of the domain. Our results show that catalytic inactivity leads to the reduction of available arginine in cells, which feeds into the NO signaling pathway. It has been shown that accumulation of NO in the cochlea protects cells from noise-induced HL (39, 40). In addition, *Prkg1* and *Pde5*, the two essential molecules of the cGMP signaling cascade, are highly expressed in outer and inner hair

cells. The cGMP-*Prkg1* signaling had a protective role against cell damage by noise-induced HL in mice, exemplified by the administration of a PDE5 inhibitor to enhance cGMP (40).

While NO signaling is widespread in mammalian physiology, the selective impact of *CPD* deficiency on the auditory system is striking. The cochlea lacks regenerative capacity and relies on tightly regulated signaling mechanisms for cochlear cell survival and function. In contrast, other tissues may be protected by functional redundancy from alternative enzymes or compensatory/repair metabolic pathways (41, 42). Thus, the auditory system may represent a unique site affected by subtle perturbations in arginine metabolism.

Mutations in a few genes have been shown to initiate ER stress and UPR, leading to HL. *GJB2* or *GJB6* mutant proteins can become trapped in the ER, preventing these gap junction proteins from transferring to the plasma membrane (43, 44). Similarly, levels of the anti-apoptotic protein Bip were elevated in the cells overexpressing pathogenic *GJB3* variants (45). *CDH23*, *USH1C*, and *MYO7A* are involved in the preassembly of the Usher protein complex at the ER in zebrafish hair cells, and defects in any one of the three proteins can induce ER stress, triggering apoptosis (46). Very recently, germline mutations in *ATF6*, a key regulator of UPR, have been reported to cause SNHL in humans and mice (47). Our study links NO deficiency with metabolic stress that induces ER stress and the UPR pathway, leading to HL.

We show that this type of HL is potentially treatable if the cellular stress is reversed by the supplementation of arginine. The addition of L-Arginine to the media rectifies NO and cGMP levels and apoptosis in patients' fibroblasts. Moreover, treating *Drosophila* CPD deficiency models with L-Arginine or sildenafil improves their gravity sensing, as shown by enhanced negative geotactic behavior, a process that requires the hearing organ JO, highlighting the

beneficial effects of modulating NO pathways for improving the function of sensory-motor neurocircuitry.

This study combines human genetics with mechanistic validation in patient-derived fibroblasts, cochlear explants, and *Drosophila*, providing a comprehensive view of *CPD* deficiency as a cause of HL. The use of cross-species modeling and demonstration of rescue via L-arginine or sildenafil highlights the therapeutic potential of targeting the NO pathway. Limitations include the lack of a mammalian *in vivo* model demonstrating auditory behavior and the relatively small number of affected individuals with biallelic variants. However, heterozygous loss-of-function variants in *CPD* may be a more common risk factor for SNHL with increasing age. Future work will focus on developing cellular and vertebrate models for *in vivo* auditory testing and evaluating combinatorial therapies involving metabolic supplementation and gene delivery.

METHODS

Sex as a biological variable

Our study included both male and female patients. We used both male and female mice in the experiments. Sex is not a biological variable.

Enrollment of participants

After enrollment, participants underwent a comprehensive clinical assessment to evaluate HL and related findings. Audiological examinations were performed in a soundproof room following standard procedures (48). We collected detailed medical and family histories, conducted thorough physical examinations, including neurological and ophthalmological assessments, and obtained laboratory and radiological tests to identify the cause of HL.

Molecular analysis

After excluding *GJB2* variants by Sanger sequencing, we initially performed ES in the probands of each family (IV:3, II:1, and II:1 in families 1, 2, and 3, respectively). Subsequently, for a comprehensive evaluation of coding and non-coding variants, we performed genome sequencing GS in the proband of family 1. Details of bioinformatic analyses and variant prioritization are provided in the Supplementary File.

Enrichment and prioritization of protein altering variants in CPD from a large cohort

We queried genome sequencing data from 65,523 participants in the 100KGP with rare diseases or cancer, aligned to the GRCh38 build. Participants were searched for inclusion under the 'hearing and ear disorders' category within their normalized disease group. Additionally, we searched for participants with any HL phenotype referenced in the free text of any HPO or ICD-10 term. Individuals not classified by 100KGP under 'hearing and ear disorders' but with identified HL phenotypes were grouped accordingly.

This process identified a total of 3,802 unrelated probands with HL. Controls consisted of 27,503 participants recruited under other disease categories without any associated HL phenotype. Relatives were excluded from the analysis. Cases and controls were matched for age, sex and ancestry.

Briefly, four categories of variants in the *CPD* gene were analyzed: (1) Protein-altering variants included those classified by functional annotations such as frameshift variants, stop-gained variants, and missense variants. No filtering was applied for MAF or *in silico* prediction tools. (2) LoF variants included predicted damaging variants such as stop-gained, splice-acceptor, and splice-donor variants, all of which were considered rare and damaging. (3) Prioritized missense

variants were restricted to those with an MAF < 0.001 and either a CADD score \geq 25 or an AlphaMissense score indicating probable damage or ambiguity (\geq 0.34). Finally, (4) combined variants included those meeting the criteria for both prioritized missense and LoF categories.

For each variant category, alternate allele counts (AC) and total allele numbers (AN) were calculated for cases and controls. Frequencies were expressed as proportions of alternate alleles to total alleles. OR were calculated to evaluate the association between variant presence and hearing loss, along with 95% confidence intervals (CIs). Fisher's Exact Test was used to compute p-values, and statistical significance was defined as p< 0.05. Analyses were performed using standard statistical software.

Protein modelling

Homology modelling of human CP-domain 2 (residues 501-875) of the wild-type CPD and the variant p.Met563Arg (family 1)/ p.Arg833His (family 2)/ p.Gln791Arg (family 3) triplet in complex with peptidomimetic inhibitor GEMSA were built using MODELLER (49). The crystal structure of duck CP-domain 2 bound to GEMSA (PDBID: 1H8L) was used as a template having sequence identity close to 85%. A total of 100 atomic models were calculated and the best structure with the lowest energy, determined by the MODELLER Objective Function, was selected for further analysis. The structural models were rendered using RIBBONS (50).

Localization of CPD in mouse inner ear and antibody validation

To assess the localization of CPD, tympanic bullae containing cochlea were dissected from P0 C57BL/6 wild-type mice. They were locally perfused with 4% paraformaldehyde through the round and oval windows and kept at 4°C overnight. Next day the cochleae were rinsed in 1× phosphate-buffered saline and permeabilized with 0.25% Triton X-100. Blocking was done in 5%

bovine serum albumin for 1 hour at room temperature. Incubation was done overnight at 4°C with primary antibodies, rabbit anti-CPD polyclonal antibody (Invitrogen, USA, Cat# CPD PA5-103707), mouse anti-MYO7A monoclonal antibody (MYO7A 138-1, Developmental Studies Hybridoma Bank at the University of Iowa), and a chicken anti-neurofilament polyclonal antibody (Milliopre-Sigma, USA, Cat# AB5539). Nuclei were stained with DAPI and images were captured with Zeiss LSM710 or Zeiss LSM 980 with AiryScan 2 confocal microscope (Carl Zeiss, OKO, Germany).

The sensitivity of rabbit anti-CPD polyclonal antibody was tested and validated in CRISPR/Cas9 mediated CPD-KO in HEK293 (ATCC, CRL-1573). *CPD* knock-out lines clone 5,14 and 55, were prepared using 5'-GAATCACAAACGGCGCACAT-3' and 5'-CGGCGCACATTGGTATGATG-3' guides and validated as described (51). The Sanger validated clones (Supplementary figure 12) were grown in Dulbecco's Modified Eagle's Medium (DMEM) supplemented with 10% FBS and 1×Normocin at 37°C, 5% CO₂, and 95% humidity. Upon reaching a 70% confluency, cells were fixed with 4% paraformaldehyde in PBS for 30 min at room temperature, followed by permeabilization with 0.3% Triton X-100 in PBS for 10 min, and then stained with rabbit anti-CPD primary antibody overnight. The following day, cells were incubated with anti-rabbit Alexa Fluor 488 secondary antibody (Invitrogen, USA, Cat# A-11008) and DAPI, respectively. Images were captured using a Zeiss LSM980 AiryScan2 confocal microscope.

Additionally, cells were transfected with (*CPD* pcDNA3.1+/C-(K)DYK[(NM_001304.4) Genscript, USA]) expression plasmid using the jetPRIME transfection reagent (Polyplus, France). After 72 h, cells were fixed with 4% paraformaldehyde in PBS for 30 min at room temperature, permeabilized with 0.5% Triton X-100 in PBS for 10 min, and then co-stained with mouse monoclonal FLAG-tag (Cell Signaling Technology, USA, Cat# 8146S) and rabbit polyclonal CPD

primary antibodies overnight. The following day, cells were incubated with anti-mouse Alexa Fluor 488 (Invitrogen, USA, Cat# A-11001) and anti-rabbit Alexa Fluor 555 (Invitrogen, USA, Cat# A-21428) secondary antibodies, respectively. Subsequently, the cells were counterstained with DAPI and mounted in Prolong Glass antifade solution (Invitrogen, Rockville, MD, USA). Images were acquired using a 63x objective on a Zeiss LSM 980 AiryScan 2 confocal microscope.

CPD enzyme activity

To measure the C-terminal cleavage activity of the carboxypeptidase D, the enzyme was incubated with the fluorescent substrate dansyl-Phe-Ala-Arg (Bachem, USA, Cat# 4028360.0005). Briefly, HEK293 cells were grown and maintained in DMEM supplemented with 10% FBS and 1×Antibiotic-antimycotic solution at 37°C, 5% CO₂ and 95% humidity. Upon 70-80% confluency, the cells were transfected with the CPD expression plasmid (GeneCopeia, Rockville, MD, USA, EX-OHU10876D) using jetPRIME transfection reagent. The mutated constructs (CPD^{c.1688T>G}, CPD^{c.2372A>G}, CPD^{c.2498G>A}) were generated using QuickChange Lightning Site-Directed Mutagenesis kit (Agilent Technologies, USA, Cat# 210518). After 72 hours of transfection, cells were harvested and lysed in 100 mM Tris-acetate (pH 6.4) containing 100 mM NaCl. 100 µL of supernatant in a microcentrifuge tube was incubated with 0.2 mM of substrate for 60 min at 37 °C. The reaction was stopped by adding 50 µL of 500 mM HCl and 1 mL of chloroform. Tubes were mixed and centrifuged for 2 min at 300xg. When centrifugation was complete, the bottom phase was separated into a fresh tube and dried overnight at room temperature in the dark. Dried samples were resuspended in 200 μL of PBS containing 0.1% Triton X-100. Fluorescence was measured at 495/350 nm using a 96-well microplate reader (Synergy H1m Monochromator-Based Multi-Mode Microplate Reader) with Gen5TM 2.0 data analysis software.

The impaired enzyme activity was also confirmed by peptidomics analysis at Creative Proteomics (NY, USA).

Fibroblast studies and effects of L-Arginine supplementation

Fibroblasts from six controls and four patients were plated in 150 × 20 mm cell culture petri dishes (Thermo Scientific, USA, Cat# 150468) using DMEM for SILAC (Thermo Scientific, Cat# A33822) supplemented with 10% dialyzed FBS (Thermo Scientific, Cat# 26400044) and 1× antibiotic-antimycotic solution. The medium was changed each alternate day, and cells were kept growing until 80% confluent. The cells were harvested in 100 μL Arginine assay buffer provided with the Arginine Assay Kit (Abcam, UK, Cat# AB252892). Cells were homogenized and centrifuged at 10000xg for 10 min at 4°C. Supernatant was prepared, and reagents were added as described by the manufacturer. The final incubation was at 37°C for 1 hour. Fluorescence was measured at 535/587 nm on a microplate reader in endpoint mode.

Similarly, for measuring intracellular Lysine, cells were collected in 100 µL Lysine assay buffer provided with Lysine assay kit (Cell Biolabs, Inc. USA, Cat# MET-130). Cells were lysed and centrifuged as above, and fresh lysates were used for the experiment. Standards were freshly prepared, and lysates from the respective groups were incubated with the colorimetric probe as described by the manufacturer. Readings were measured with a spectrophotometric plate reader at 550nm.

For NO and cGMP measurements, upon 80% confluency, the media was supplemented with 6 mM L-Arginine (Thermo Scientific, Cat# A14730.22) for 48 hours. Cells were harvested after 48 hours and homogenized in RIPA buffer (Thermo Scientific, Cat# 89900) mixed with 1×HaltTM protease and phosphatase inhibitor cocktail (Thermo Scientific, Cat# 78441). Each sample was then

centrifuged at 12,000 g for 15 min at 4°C. The supernatant was collected, protein estimation was conducted via bicinchoninic acid assay (Sigma-Aldrich, Cat# B9643), and absorbance was measured at 562 nm using a microplate reader. For NO measurement, incubation was done for 10 min at 60°C, and absorbance was measured at 540 nm according to an NO assay kit (Abcam, Cat# ab272517). For cGMP levels, cells were harvested after 48 hours in 0.1M HCl and hydrolyzed to obtain total cell lysates. The absorbance was measured at 412 nm in a 96-well ELISA plate (Cayman, USA, Cat# 581021). Raw data were analyzed using the provided web tool (https://www.myassays.com/cyclic-gmp-acetylated.assay).

Apoptosis detection assays

Apoptosis was observed with TUNEL staining of patient's fibroblasts. Approximately 5×10⁴ cells were plated on glass coverslips and TUNEL assay was performed using the one step TUNEL in situ apoptosis kit (Biotium, USA, Cat# 30063) according to the manufacturer's protocol. Images were quantified using ImageJ software (NIH, USA). The images were split into respective channels, and thresholding was done to highlight only the cells. The count particle function was used to get the number of cells detected in each channel. % apoptosis cells were calculated and plotted using GraphPad Prism software (version 10.0.2).

Fibroblasts from patients and control samples were also tested for apoptosis using flow cytometry. Cells were collected, washed with PBS and stained with Annexin V-FITC/PI detection kit (Biolegend, USA, Cat# 640914). Stained cells were analyzed using FACS Aria IIu Flow Cytometer and data were processed using FlowJo software. Gating details are provided in the supplementary file.

Additionally, we performed Western blot analysis to investigate the role of conventional proteins for apoptosis in patients and control fibroblasts. Cells were harvested in RIPA lysis buffer, and the extracted proteins were resolved through a 4-20% Tris-Glycine gradient gel and then transferred to a 0.22 µm PVDF membrane. The membrane was then blocked in 5 % BSA for 1 hour and incubated overnight at 4°C with primary antibodies ERK1/2 (Cell signaling Technology, USA, Cat# 9532S), pERK1/2 (Cell signaling Technology, USA, Cat# 5625S), AKT (Cell signaling Technology, USA, Cat# 9272S); pAKT (Cell Signaling Technology, USA, Cat# 4060S), BAD (Cell signaling Technology, USA, Cat# 9239S); pBAD (Cell Signaling Technology, USA, Cat# 4366S/9291S), CREB (Cell signaling Technology, USA, Cat# 4820S); pCREB (Cell signaling Technology, USA, Cat# 9198S), and Caspases-3 (Cell signaling Technology, USA, Cat# 14220S) each diluted at 1:1000 in 5 % BSA + TBST (TBS with 0.5% Tween). The next day, the membrane was washed and incubated with anti-rabbit or anti-mouse peroxidase-conjugated secondary antibody (1:3000) and developed using West Pico Super-Signal ECL substrate (Thermo Scientific, USA, 37069). Finally, visualization was performed using FluorChemE (ProteinSimple, USA). Quantification was done using ImageJ software.

Oxidative stress in control and patient fibroblasts was measured with H₂DCFDA (Thermo Scientific, USA, Cat# D399) fluorometric assay. Approximately 7000 cells were seeded in 96-welll cell culture plates. After 24 hours, the cells were loaded with 100 µL of 10 µM H₂DCFDA and incubated for 30-40 minutes at 37°C. Subsequently, cells were washed, and volume was replaced with pre-warmed HBSS. The plate was read at ex/em 485/535 as discussed earlier.

Mitochondrial membrane potential is a good indicator of the healthy state of cells. To observe the mitochondrial dysfunction in control and patients' fibroblasts, the cells were maintained as discussed above. A 1:1000 working solution of JC-1 (Cell Signaling Technology, USA, Cat#

92891), a ratio-metric fluorescent reporter of mitochondrial membrane potential, was prepared according to manufacturer's protocol to stain the cells following an incubation for 30 minutes. Cells were washed and passed through a cell strainer before the FACS analysis. FACS Aria IIu Flow Cytometer with lasers (488 and 561 nm), and filters (525/50 and 585/42 nm) were used, and data were processed using FlowJo software. Details of the gating strategy are given in the supplementary file.

ER stress markers quantification

Spliced *XBP1* (s*XBP1*), associated with pro-homeostatic activity of the UPR and CHOP, correlated with pro-apoptotic activity of the UPR and was tested and quantified in cultured fibroblasts. Briefly, cells were grown as described earlier. RNA was extracted when cells reached 70-80% confluency. Spliced and unspliced forms of *XBP1* were measured by semi-quantitative PCR and qPCR and quantified against *GAPDH*. Densitometric analysis was performed using ImageJ, and intensities were recorded for further statistical analysis.

The lysates from the fibroblasts were prepared for Western blot analysis as described in the previous section. The membranes were incubated with anti-rabbit CHOP primary antibody (Proteintech, USA, Cat# 15204-1-AP) (1:1500) overnight, and blots were developed after staining with the respective secondary antibody. Quantification was performed using ImageJ analysis software, and plots were generated for relative levels of CHOP in both controls and patients, normalized to GAPDH.

Organotypic cultures of mouse cochlea and Cpd silencing

C57BL/6 mice were time mated to obtain E13.5 embryos. Cochleae from embryos confirming E13.5 staging criteria were used for culture. Dissection was performed as described (52), and 4

cochleae were placed on each Millicell cell culture insert. Cpd RNAi lentiviral system (sc-142542-V, sc-108080 (control), and sc-142542-PR) was purchased from Santa Cruz Biotechnology, Inc. After 3 days of culture, cochleae were transduced with viral particles at 1×10^6 , 2×10^6 , and 4×10^6 multiplicity of infection (MOI). The media was changed the following day, and cochlea was cultured until E18.5. The efficiency of transduction was measured with qPCR and fold change in Cpd expression was determined. To quantify the apoptosis in cochlear cells, the tissue was harvested at E18.5, fixed, and a one-step TUNEL assay was performed. MYO7A, SOX2, and CPD antibodies were used to detect any differences in lateral and medial domains of silenced and wildtype specimens. Imaging was performed using a Zeiss LSM 980 microscope equipped with a 63×/1.4 NA oil-immersion objective. Z-stacks were acquired with tiling using a zoom factor of 1.2× and a frame size of 2048×2048 pixels. All images were captured with consistent laser power, gain, and offset settings. Maximum intensity projections were generated from z-stacks using ImageJ. To quantify apoptosis, three regions of interest (ROIs) from the apical mid and basal turns in each image, encompassing the cochlear sensory epithelium, were manually selected. The "Threshold" function was applied to the green channel to identify TUNEL-positive cells using consistent settings across all images. The number of apoptotic cells was quantified using the "Analyze Particles" tool with size and circularity parameters optimized to exclude background noise. The number of TUNEL-positive cells was normalized to the total number of DAPI-stained nuclei within the same ROI to calculate the percentage of apoptotic cells.

The effect of arginine supplementation to overcome apoptosis in the cochlea was also tested. Briefly, the culture was done as mentioned earlier; however, the cochleae were kept in a modified media comprised of DMEM for SILAC supplemented with 10% dialyzed FBS, 1×N-2 supplement (ThermoFisher Scientific, USA, Cat# 17502001), 1×B-27 (minus antioxidants) (ThermoFisher

Scientific, USA, Cat# 10889038), and 1×penicillin. We tested three different concentrations of arginine (3mM, 5mM, and 6mM) to evaluate the effective dose for the rescue of apoptosis in the cochlea (data not shown). After repeated experimentation and analysis, we selected 5mM arginine as the best dose to be added at E17.5 for 24 hours. The tissue was harvested at E18.5, fixed, and stained for apoptotic and sensory epithelial markers. Quantification and statistical analysis of images from 3 ROIs on each cochlea (n=4) was done using ImageJ and GraphPad Prism.

Drosophila studies using the automated geotaxis monitoring platform

elav^{C155}-Gal4, svr^I , and UAS-silver-RNAi strains previously generated and confirmed were obtained from the Bloomington stock center (53). Fly strain canton-s (cs) and UAS-luciferase-RNAi were used as controls. Behavior assay was performed on an automated behavior monitoring system as previously published (54). Briefly, each behavior cylinder was preloaded with \leq 7 flies, and the geotaxis of each fly was recorded with a digital camera (ImagingSource LLC, model no. DMK23U445). The two-dimensional positions (x, y coordinates) of individual flies (maximum height, 14 cm) at 33 millisecond resolution (30 fps) were determined and tracked. Finally, the difference in SD of horizontal and vertical positions was used to calculate movement direction. Specifically, for a given fly, movement direction = (SD of y coordinates – SD of x coordinates)/(SD of y coordinates + SD of x coordinates). Matlab (Mathworks) was used for analysis.

Wholemount of Drosophila Johnston's Organ

Antennae were detached from the heads and fixed in freshly made 4% formaldehyde (in Phosphate buffered saline, PBS, pH7.4) with 0.01% PBTx (PBS containing 0.4% v/v Triton X-100) for 20 min. The antennas were then washed with 0.4% PBTx three times for 15 minutes. Incubated overnight with Alexa 546 conjugated Phalloidin (Invitrogen, A22283, 1:200) diluted

in 0.4% PBTX with 5% normal goat serum at 4 °C, followed by DAPI (Invitrogen, D1306, 1:300) staining for 10 min. After washing, tissues were mounted with VECTASHIELD Antifade Mounting Medium (Vector Laboratories) and imaged. Slides were imaged using an Olympus FV4000 confocal microscope with a 60x oil immersion objective lens with 2.0x zoom, with a scan speed of 2.0us per pixel and spatial resolution of 2048x2048 pixels. Images were processed using cellSens FV.

Sound-evoked potentials of Drosophila Antenna

Sound-evoked potentials (SEPs) were captured using a pair of electrolytically sharpened tungsten recording electrodes (55, 56). The recording electrode was inserted between the first and second antennal segments, while the reference electrode was inserted into the head cuticle near the posterior orbital bristle. A computer-generated pulse song was introduced frontally to the fly under near-field conditions. Signals were subtracted and amplified with a differential amplifier (DAM50, World Precision Instruments) and digitized at 10 kHz (USB-6001, National Instruments). Average response values were measured as the max-min values in an averaged trace from 10 consecutive presentations of the described protocol.

Statistical analysis

Statistical analysis was performed by applying Tukey's multiple comparison test. One-way *ANOVA* with Dunnett's or Sidak's multiple comparison test or two-way *ANOVA* with Tukey's multiple comparison test was used to compare multiple groups. $p \le 0.05$ was considered statistically significant. All statistical analyses were performed in GraphPad Prism software (version 10.0.2 or version 10.0.3).

Study Approval

The experimental procedures were approved by the local institutional review boards (Protocol# 20081138, USA, and Protocol# 012413, Türkiye). All participants (or parents/guardians) provided written informed consent in accordance with the Declaration of Helsinki protocol.

Wild-type C57BL/6 mice were bred and maintained at the University of Miami, where all procedures were approved by the Institutional Animal Care and followed the NIH Guidelines, "Using Animals in Intramural Research".

Supplemental information

This article contains supplementary information comprised of supplementary methods, figures, and tables. All supporting data values underlying the figures in this manuscript are provided in the Supporting Data Values file.

Data availability statement

Genome and exome sequencing data were deposited in the NCBI's BioProject database: Exome sequencing project PRJNA1079783, samples SAMN40082632 (Family_1_IV:3_exome), SAMN40082633 (Family_2_II:1_exome) and SAMN40082634 (Family_3_II:1_exome). Genome sequencing project PRJNA1079835, sample SAMN40090193 (Family1_IV:3_Genome). Primary data from the 100KGP database are held in a secure Research Environment and available to registered users. Other data generated or analyzed during this study are included in this article and its supplementary information files.

Acknowledgments

We are grateful to the participating families included in this study. We thank all physicians, genetic counselors, and audiologists for providing all the relevant information. This research was made possible through access to data in the National Genomic Research Library, which is managed by Genomics England Limited (a wholly owned company of the Department of Health and Social Care). The National Genomic Research Library holds data provided by patients and collected by the NHS as part of their care and data collected as part of their participation in research. The National Genomic Research Library is funded by the National Institute for Health Research and NHS England. The Wellcome Trust, Cancer Research UK and the Medical Research Council have also funded research infrastructure. We are also thankful to the Flow Cytometry Shared Resource (FCSR) of the Sylvester Comprehensive Cancer Center at the University of Miami, RRID:

SCR022501, for confocal microscopy and flow cytometry services. This work is the result of NIH funding and is subject to the NIH Public Access Policy. Through acceptance of this federal funding, the NIH has been given a right to make the work publicly available in PubMed Central.

Funding

This work was supported by NIH R01DC009645 and R01DC012836 to MT, NIH R33AT010408 to RGZ, and ANPCyT Argentina PICT-2021 GRF-TI-00422 to KW. N.V was supported by the American Heart Association postdoctoral fellowship (23POSTCHF1031213).

Author contributions

Conceptualization: M.R and M.T, Data collection: M.R, M.F.Z, A.G.L., N.O.-V., C.A, A.F, N.V, M.T, N.B, S.G, S.T.-Y, M.K.-Y, V.C, M.C.R, T.C, M.A.J, Formal analysis: M.R, G.B, S.G, N.V, D.D, A.G.L., N.O.-V., C.A, A.F., F.E.T. Funding acquisition: M.T, R.G.Z., K.W, Writing original draft: M.R and M.T, Writing-review and editing: M.R, A.G.L., N.O.-V., M.F.Z, C.A, T.A, N.B, S.G, S.T.-Y, M.K.-Y, S.G, E.A.D, M.A, S.S, G.B, N.V, D.D, G.W, I.K, A.F, D.F.E, J.N, K.W, R.G.Z, M.T.

Ethics declaration

The study was approved by the Institutional Review Board at University of Miami, USA, Ankara University Medical School Ethics Committee, Türkiye.

Conflict of interest

Authors declare no conflict of interest.

References

- 1. Tucci DL, Merson MH, Wilson BS. A summary of the literature on global hearing impairment: current status and priorities for action. Otol Neurotol. 2010;31(1):31-41.
- 2. Yueh B, Shapiro N, MacLean CH, Shekelle PG. Screening and management of adult hearing loss in primary care: scientific review. JAMA. 2003;289(15):1976-85.
- 3. Fritzsch B, Elliott KL. Gene, cell, and organ multiplication drives inner ear evolution. Dev Biol. 2017;431(1):3-15.
- 4. Stuehr DJ, Haque MM. Nitric oxide synthase enzymology in the 20 years after the Nobel Prize. Br J Pharmacol. 2019;176(2):177-88.
- 5. Sidyelyeva G, Fricker LD. Characterization of Drosophila carboxypeptidase D. The J Biol Chem. 2002;277(51):49613-20.
- 6. Shen J, Harada N, Yamashita T. Nitric oxide inhibits adenosine 5'-triphosphate-induced Ca2+ response in inner hair cells of the guinea pig cochlea. Neurosci Lett. 2003;337(3):135-8.
- 7. Shen J, Harada N, Nakazawa H, Kaneko T, Izumikawa M, Yamashita T. Role of nitric oxide on ATP-induced Ca2+ signaling in outer hair cells of the guinea pig cochlea. Brain Res. 2006;1081(1):101-12.
- 8. Reuss S, Riemann R. Distribution and projections of nitric oxide synthase neurons in the rodent superior olivary complex. Microsc Res Tech. 2000;51(4):318-29.
- 9. Heinrich U-R, Maurer J, Mann W. Evidence for a possible NOS back-up system in the organ of Corti of the guinea pig. Eur Arch Otorhinolaryngol. 2004;261(3):121-8.
- 10. Vyas P, Wu JS, Jimenez A, Glowatzki E, Fuchs PA. Characterization of transgenic mouse lines for labeling type I and type II afferent neurons in the cochlea. Sci Rep. 2019;9(1):5549.
- 11. Fessenden JD, Altschuler RA, Seasholtz AF, Schacht J. Nitric oxide/cyclic guanosine monophosphate pathway in the peripheral and central auditory system of the rat. J Comp Neurol. 1999;404(1):52-63.
- 12. Coomber B, Berger JI, Kowalkowski VL, Shackleton TM, Palmer AR, Wallace MN. Neural changes accompanying tinnitus following unilateral acoustic trauma in the guinea pig. Eur J Neurosci. 2014;40(2):2427-41.
- 13. Hockley A, Berger JI, Palmer AR, Wallace MN. Nitric oxide increases gain in the ventral cochlear nucleus of guinea pigs with tinnitus. Eur J Neurosci. 2020;52(9):4057-80.

- 14. Cao X-J, Lin L, Sugden AU, Connors BW, Oertel D. Nitric Oxide-Mediated Plasticity of Interconnections Between T-Stellate cells of the Ventral Cochlear Nucleus Generate Positive Feedback and Constitute a Central Gain Control in the Auditory System. J Neurosci. 2019;39(31):6095-107.
- 15. Lee J-J, Cho Y-W, Huh Y, Cha CI, Yeo SG. Effect of nitric oxide on auditory cortical neurons of aged rats. Neurosci Lett. 2008;447(1):37-41.
- 16. Gotoh T, Mori M. Nitric oxide and endoplasmic reticulum stress. Arterioscler Thromb Vasc Biol. 2006;26(7):1439-46.
- 17. Takuma K, Yan SS, Stern DM, Yamada K. Mitochondrial dysfunction, endoplasmic reticulum stress, and apoptosis in Alzheimer's disease. J Pharmacol Sci. 2005;97(3):312-6.
- 18. Dickhout JG, Hossain GS, Pozza LM, Zhou J, Lhoták Sar, Austin RC. Peroxynitrite causes endoplasmic reticulum stress and apoptosis in human vascular endothelium: implications in atherogenesis. Arterioscler Thromb Vasc Biol. 2005;25(12):2623-9.
- 19. Kochhar A, Hildebrand MS, Smith RJ. Clinical aspects of hereditary hearing loss. Genet Med. 2007;9(7):393-408.
- 20. Lv J, Wang H, Cheng X, Chen Y, Wang D, Zhang L, et al. AAV1-hOTOF gene therapy for autosomal recessive deafness 9: a single-arm trial. Lancet (London, England). 2024.
- 21. Caulfield M, Davies J, Dennys M, Elbahy L, Fowler T, Hill S, et al. National Genomic Research Library. figshare; 2020.
- 22. Hadkar V, Skidgel RA. Carboxypeptidase D is up-regulated in raw 264.7 macrophages and stimulates nitric oxide synthesis by cells in arginine-free medium. Mol Pharmacol. 2001;59(5):1324-32.
- 23. Mejía-García TA, Portugal CC, Encarnação TG, Prado MAM, Paes-de-Carvalho R. Nitric oxide regulates AKT phosphorylation and nuclear translocation in cultured retinal cells. Cellular Signal. 2013;25(12):2424-39.
- 24. Luiking YC, Ten Have GA, Wolfe RR, Deutz NE. Arginine de novo and nitric oxide production in disease states. Am J Physiol Endocrinol Metab. 2012;303(10):E1177-E89.
- 25. Lin X, Li S, Zou Y, Zhao F-Q, Liu J, Liu H. Lysine stimulates protein synthesis by promoting the expression of ATB0,+ and activating the mTOR pathway in bovine mammary epithelial cells. J Nutr. 2018;148(9):1426-33.

- 26. Ali YO, Escala W, Ruan K, Zhai RG. Assaying locomotor, learning, and memory deficits in Drosophila models of neurodegeneration. J Vis Exp. 2011(49):2504.
- 27. Sidyelyeva G, Baker NE, Fricker LD. Characterization of the molecular basis of the Drosophila mutations in carboxypeptidase D. Effect on enzyme activity and expression. J Biol Chem. 2006;281(19):13844-52.
- 28. Li C, Bademci G, Subasioglu A, Diaz-Horta O, Zhu Y, Liu J, et al. Dysfunction of GRAP, encoding the GRB2-related adaptor protein, is linked to sensorineural hearing loss. Proc Natl Acad Sci U S A. 2019;116(4):1347-52.
- 29. Li T, Giagtzoglou N, Eberl DF, Jaiswal SN, Cai T, Godt D, et al. The E3 ligase Ubr3 regulates Usher syndrome and MYH9 disorder proteins in the auditory organs of Drosophila and mammals. Elife. 2016;5.
- 30. Li T, Bellen HJ, Groves AK. Using Drosophila to study mechanisms of hereditary hearing loss. Dis Model Mech. 2018;11(6).
- 31. Li H, Janssens J, De Waegeneer M, Kolluru SS, Davie K, Gardeux V, et al. Fly Cell Atlas: A single-nucleus transcriptomic atlas of the adult fruit fly. Science. 2022;375(6584):eabk2432.
- 32. Boekhoff-Falk G, Eberl DF. The Drosophila auditory system. Wiley Interdiscip Rev Dev Biol. 2014;3(2):179-91.
- 33. Senthilan PR, Piepenbrock D, Ovezmyradov G, Nadrowski B, Bechstedt S, Pauls S, et al. Drosophila auditory organ genes and genetic hearing defects. Cell. 2012;150(5):1042-54.
- 34. Pézier AP, Jezzini SH, Bacon JP, Blagburn JM. Shaking B mediates synaptic coupling between auditory sensory neurons and the giant fiber of Drosophila melanogaster. PLoS One. 2016;11(4):e0152211.
- 35. Gomis-Rüth FX. Structure and mechanism of metallocarboxypeptidases. Crit Rev Biochem Mol Biol. 2008;43(5):319-45.
- 36. Novikova EG, Eng FJ, Yan L, Qian Y, Fricker LD. Characterization of the enzymatic properties of the first and second domains of metallocarboxypeptidase D. J Biol Chem. 1999;274(41):28887-92.
- 37. Eng FJ, Novikova EG, Kuroki K, Ganem D, Fricker LD. gp180, a protein that binds duck hepatitis B virus particles, has metallocarboxypeptidase D-like enzymatic activity. J Biol Chem. 1998;273(14):8382-8.

- 38. Sidyelyeva G, Wegener C, Schoenfeld BP, Bell AJ, Baker NE, McBride SMJ, et al. Individual carboxypeptidase D domains have both redundant and unique functions in Drosophila development and behavior. Cell Mol Life Sci. 2010;67(17):2991-3004.
- 39. Shi X, Ren T, Nuttall AL. The electrochemical and fluorescence detection of nitric oxide in the cochlea and its increase following loud sound. Hear Res. 2002;164(1):49-58.
- 40. Alvarado JC, Fuentes-Santamaría V, Gabaldón-Ull MC, Jareño-Flores T, Miller JM, Juiz JM. Noise-induced "toughening" effect in wistar rats: enhanced auditory brainstem responses are related to calretinin and nitric oxide synthase upregulation. Front Neuroanat. 2016;10:19.
- 41. Bommer GT, Van Schaftingen E, Veiga-da-Cunha M. Metabolite Repair Enzymes Control Metabolic Damage in Glycolysis. Trends Biochem Sci. 2020;45(3):228-43.
- 42. Beaudoin GA, Hanson AD. A Guardian Angel Phosphatase for Mainline Carbon Metabolism. Trends Biochem Sci. 2016;41(11):893-4.
- 43. Zhang Y, Wang J, Li L, Sun Y, Feng B. Three common GJB2 mutations causing nonsyndromic hearing loss in Chinese populations are retained in the endoplasmic reticulum. Acta Otolaryngol. 2010;130(7):799-803.
- 44. Berger AC, Kelly JJ, Lajoie P, Shao Q, Laird DW. Mutations in Cx30 that are linked to skin disease and non-syndromic hearing loss exhibit several distinct cellular pathologies. J Cell Sci. 2014;127(8):1751-64.
- 45. Xia K, Ma H, Xiong H, Pan Q, Huang L, Wang D, et al. Trafficking abnormality and ER stress underlie functional deficiency of hearing impairment associated connexin-31 mutants. Protein Cell. 2010;1:935-43.
- 46. Blanco-Sánchez B, Clément A, Fierro Jr J, Washbourne P, Westerfield M. Complexes of Usher proteins preassemble at the endoplasmic reticulum and are required for trafficking and ER homeostasis. Dis Model Mech. 2014;7(5):547-59.
- 47. Lee E-J, Kim K, Diaz-Aguilar MS, Min H, Chavez E, Steinbergs KJ, et al. Mutations in unfolded protein response regulator ATF6 cause hearing and vision loss syndrome. J Clin Invest. 2024;135(3): e175562.
- 48. Mazzoli M, Van Camp G, Newton V, Giarbini N, Declau F, Parving A. Recommendations for the description of genetic and audiological data for families with nonsyndromic hereditary hearing impairment. Audiol Med. 2003;1(2):148-50.

- 49. Martí-Renom MA, Stuart AC, Fiser A, Sánchez R, Melo F, Šali A. Comparative protein structure modeling of genes and genomes. Annu Rev Biophys Biomol Struct. 2000;29(1):291-325.
- 50. Carson M. RIBBONS 2.0. J Appl Crystallogr. 1991;24(5):958-61.
- 51. Ramzan M, Zafeer MF, Abad C, Guo S, Owrang D, Alper O, et al. Genetic heterogeneity in hereditary hearing loss: Potential role of kinociliary protein TOGARAM2. Eur J Hum Genet. 2024;32(6):639-46.
- 52. Jacques BE, Montcouquiol ME, Layman EM, Lewandoski M, Kelley MW. Fgf8 induces pillar cell fate and regulates cellular patterning in the mammalian cochlea. Development. 2007; 134(16): 3021-9.
- 53. Lee GG, Zeng K, Duffy CM, Sriharsha Y, Yoo S, Park JH. In vivo characterization of the maturation steps of a pigment dispersing factor neuropeptide precursor in the Drosophila circadian pacemaker neurons. Genetics. 2023;225(1): 118.
- 54. Zhu Y, Lobato AG, Rebelo AP, Canic T, Ortiz-Vega N, Tao X, et al. Sorbitol reduction via govorestat ameliorates synaptic dysfunction and neurodegeneration in sorbitol dehydrogenase deficiency. JCI insight. 2023;8(10): e164954.
- 55. Eberl DF, Hardy RW, Kernan MJ. Genetically similar transduction mechanisms for touch and hearing in Drosophila. J Neurosci. 2000;20(16):5981-8.
- 56. Eberl DF, Kernan MJ. Recording sound-evoked potentials from the Drosophila antennal nerve. Cold Spring Harb Protoc. 2011;2011(3):prot5576.
- 57. Davydov EV, Goode DL, Sirota M, Cooper GM, Sidow A, Batzoglou S. Identifying a high fraction of the human genome to be under selective constraint using GERP++. PLoS Comput Biol. 2010;6(12):e1001025.
- 58. Danzi MC, Dohrn MF, Fazal S, Beijer D, Rebelo AP, Cintra V, et al. Deep structured learning for variant prioritization in Mendelian diseases. Nat Commun. 2023;14(1):4167.

Table 1: Phenotypic and genotypic details of affected individuals

Characteristic	Family 1			Family 2	Family 3
	IV:2	IV:3	IV:4	II:1	II:1
Age (years)	46	23	14	6	10
HL severity	Profound	Profound	Profound	Profound	Severe-profound
Age at diagnosis (months)	12	20	1	11	12
Cochlear implant	No	Unilateral	Unilateral	Bilateral	Bilateral
CPD c.DNA change (HGVS, NM_001304.5)	c.1688T>G			c.2498G>A	c.2372A>G
CPD protein change (HGVS, NP_001295.2)	p.(Met563Arg)			p.(Arg833His)	p.(Gln791Arg)
MAF (gnomAD v4)	Absent			0.000007	Absent
Ethnicity-matched allele frequency		0/1612		0/1612	0/1612
MAVERICK score (AR)	0.62			0.69	0.62
GERP conservation score	5.6			5.6	5.6

Abbreviations: AR: autosomal recessive **HL**; Hearing Loss, **MAF**; Minor Allele Frequency; **gnomAD**, genome aggregation database; **GERP**, Genomic Evolutionary Rate Profiling is a method for producing DNA position-specific estimates of evolutionary constraint using maximum likelihood (ranges from -12.3 to 6.17) (57) **MAVERICK**, Mendelian Approach to Variant Effect pRedICtion built in Keras is an AI-assisted method of variant pathogenicity probability (ranges between 0-1) (58).

Figures and Figure Legends:

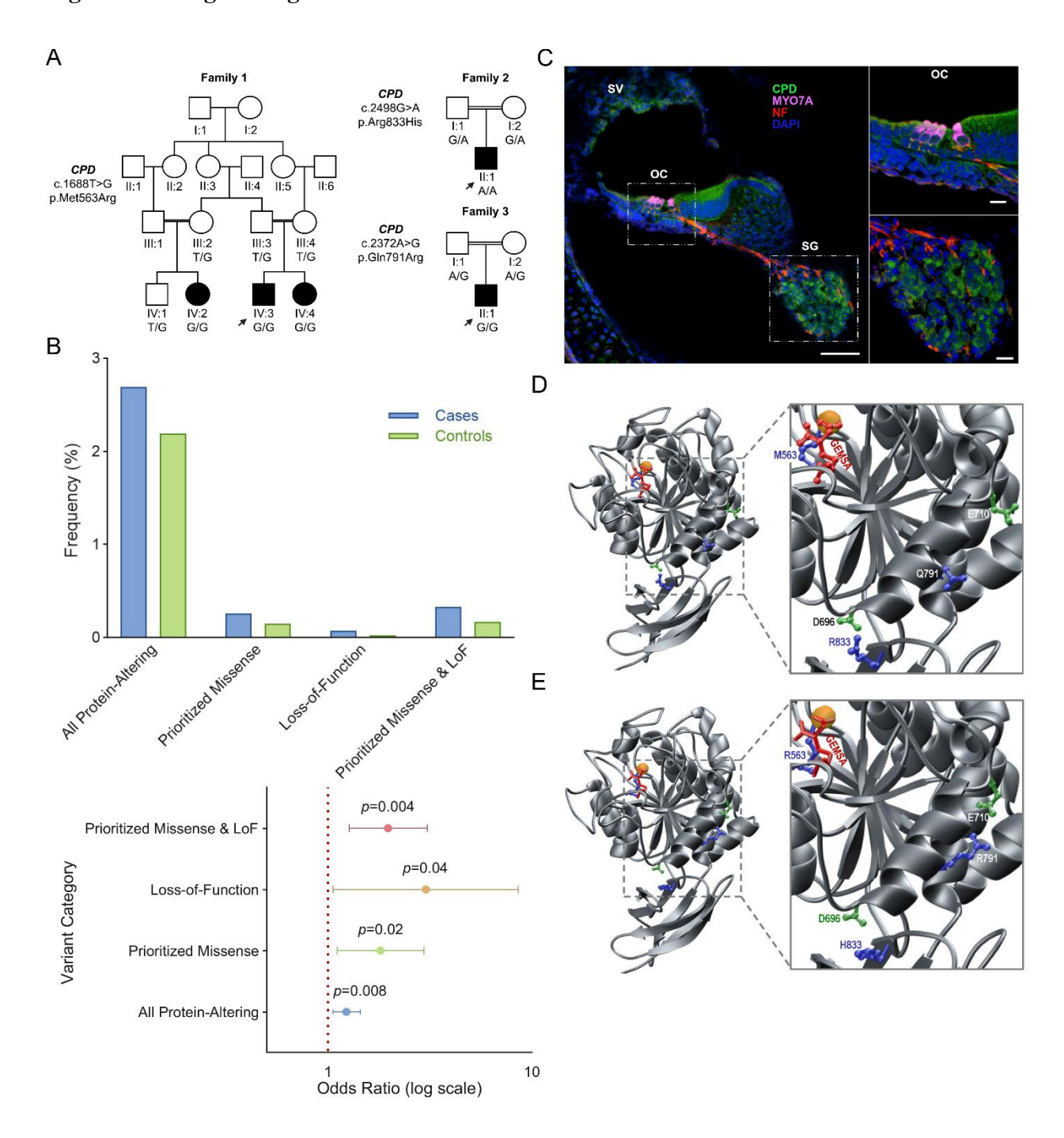


Figure 1: Pedigrees, *CPD* variant enrichment in hearing loss population, protein localization in mouse inner ear, and *in silico* effects of identified variants. **(A)** Pedigrees of three participating families and details of variant segregation in each family. Males are symbolized by squares, and

females by circles. Filled symbols indicate affected individuals, and double lines denote consanguinity. Probands in each pedigree are mentioned with an arrow. (B) Comparison of the frequency of disease-causing variants in CPD among cohorts with hearing loss and the control population. Patients exhibit a higher frequency of protein-altering (2.69% vs. 2.19%), missense (0.26% vs. 0.15%), and LoF variants (0.07% vs. 0.02%) compared to controls, suggesting a more substantial contribution of these variants to hearing loss. Similarly, the forest plot displays the odds ratios (ORs) with 95% confidence intervals (CIs) for disease-causing variants in CPD among patients with hearing loss compared to controls. The red dashed line represents an OR of 1, indicating no association. The odds ratios are significantly elevated for combined variants (OR = 1.97), LoF variants (OR = 3.02), and prioritized missense variants (OR = 1.81), confirming a strong association between CPD variants and hearing loss in patients. (C) Localization of CPD in the mouse inner ear. Representative staining of P0 cochlea section stained for CPD (green), MYO7A (magenta), Neurofilament (red), and DAPI (blue). Panels on the right are close-ups of the boxed region, outlined in white. Spiral ganglion (SG), organ of Corti (OC), and stria vascularis (SV) are marked. Note the localization of CPD at the spiral ganglion, stria vascularis, and organ of Corti. Scale bar: 60 µm; small panels at right have a scale bar of 15µm. (D-E) Ribbon representation of the structural model of the wild-type protein and the variant harboring the M563R/Q791R/R833H triplet of human CP-domain 2 (residues 501-875). Note that the CP-domain 2 is comprised of two subdomains: an N-terminal αβ-fold harboring a Zn²⁺ divalent ion (indicated by a yellow sphere) as a cofactor at the heart of the active site, followed by a C-terminal β-barrel. In each case, the entire protein backbone is colored gray. The sidechain moieties of the M563R/Q791R/R833H triplet are colored blue and, where shown, their interacting partners green. The peptidomimetic inhibitor GEMSA is colored red.

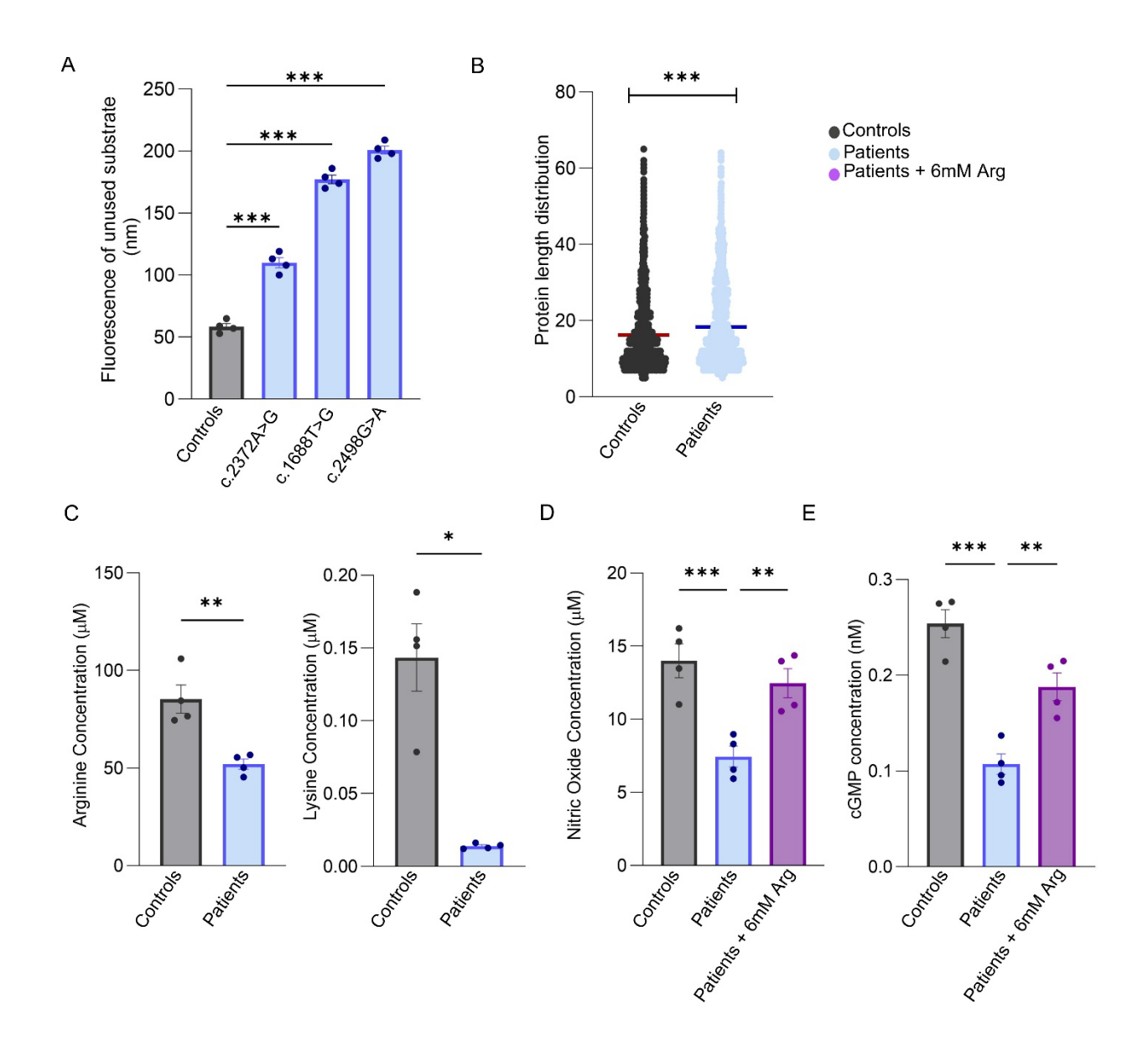


Figure 2: *In vitro* analysis of CPD variants. **(A)** The comparison of enzyme activity in mutated and control cells shows significantly reduced activity in patients, as evidenced by fluorescence-based substrate assays. **(B)** Mass spectrometry analysis revealed a difference in protein length between controls and patients in fibroblasts, with longer peptide lengths observed in patients. **(C)** Effect on the concentration of intracellular arginine and lysine in patient fibroblasts, compared to controls. **(D)** Nitric Oxide (NO) concentration measured in controls, patients, and treated groups.

(E) cGMP levels measured in controls, patients, and treated groups. The results are from 3-4 independent experiments, expressed as Mean \pm SEM. Statistical significance was determined using the unpaired t-test and ANOVA. Significant differences are denoted with asterisks (* $p \le 0.05$, ** $p \le 0.001$, *** $p \le 0.0001$) when compared to controls.

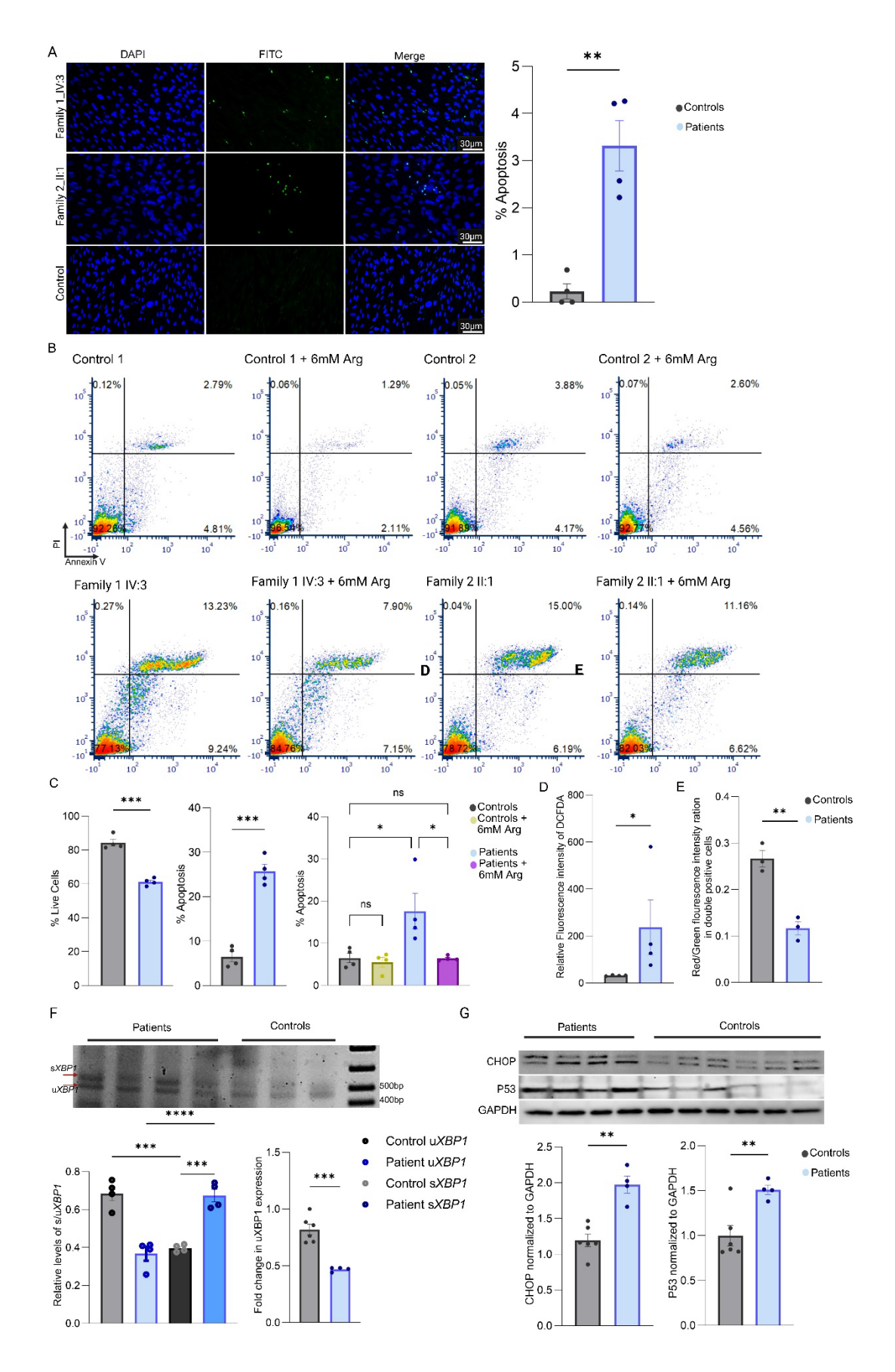


Figure 3: Analysis of apoptosis and mechanistic pathways in patient-derived fibroblasts. (A) Representative images of TUNEL staining showing increased apoptosis in patient-derived fibroblasts compared to controls, with quantification of apoptotic cells (% apoptosis, right). (B, C) Representative images of flow cytometry (B), and statistical analysis (C) of Annexin V and PI staining in patient fibroblasts (bottom row) compared to controls (top row). Arginine supplementation reduces apoptosis in patient fibroblasts, as shown in the quantification of live and apoptotic cells (far right in C). (D) Relative fluorescence intensity of H₂DCFDA indicates higher levels of oxidative stress in patient fibroblasts compared to controls. (E) JC-1 staining demonstrates altered mitochondrial membrane potential in patient fibroblasts, shown by the red/green fluorescence intensity ratio. (F) Representative gel image of XBP1 splicing via RTqPCR (top image) and densitometric analysis (bottom left graph) show elevated levels of spliced XBP1 (sXBP1) in patient fibroblasts compared to controls, confirming UPR activation. Fold change (RT-qPCR) in XBP1 expression, confirming the increase in the spliced form of XBP1 in patients. (G) Western blot analysis of UPR markers (representative gel image on top) reveals increased abundance of CHOP (bottom left graph) and p53 (bottom right graph) in patient fibroblasts, with quantification normalized to GAPDH (right). The results are from 3-4 independent experiments and expressed as Mean \pm SEM. Statistical significance was determined using the unpaired t-test and ANOVA.

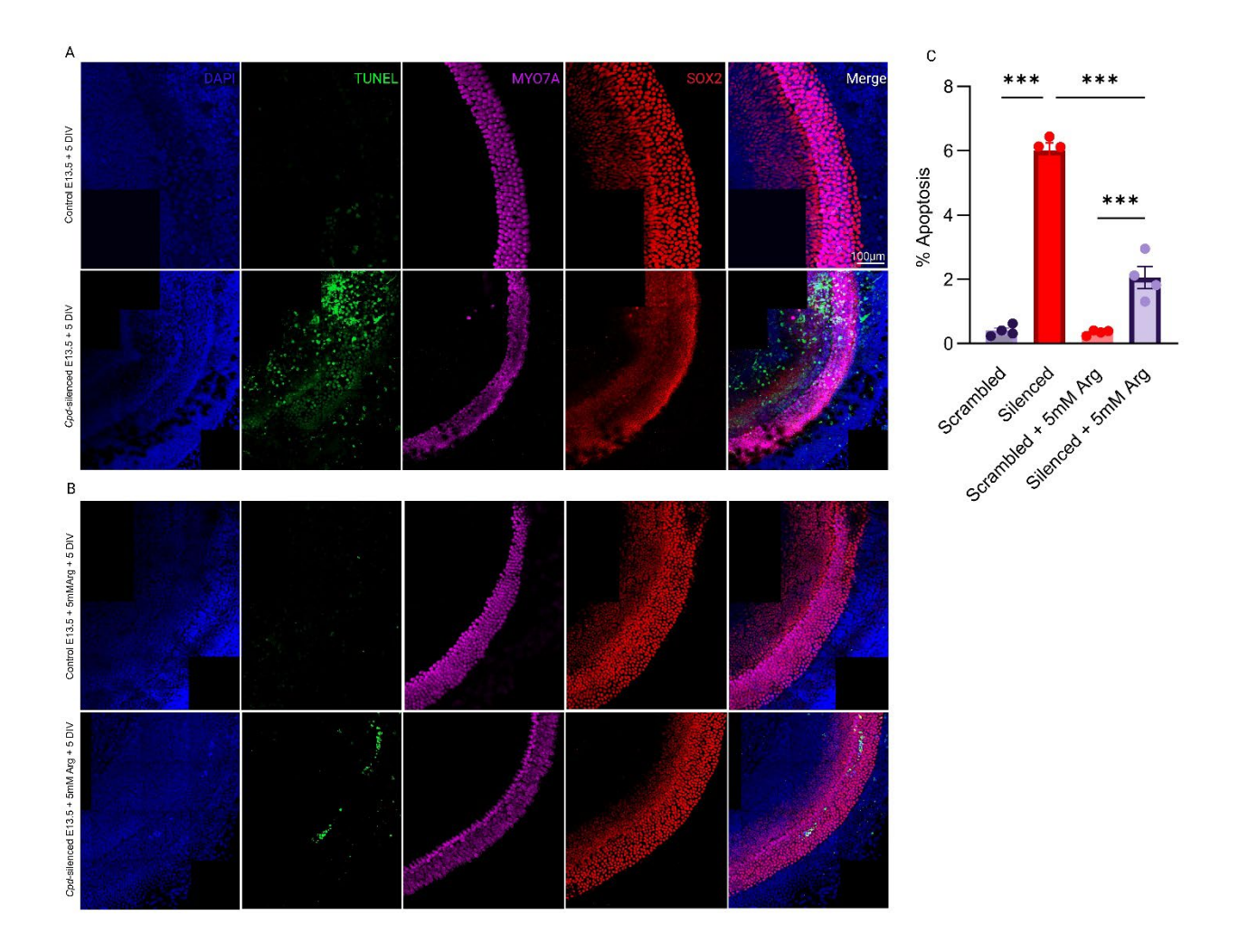


Figure 4: Silencing Cpd in the mouse cochlea enhances apoptosis rescued by arginine supplementation. (A) Representative confocal images of mouse cochlear explants (E13.5 + 5 DIV) showing increased apoptosis following Cpd silencing (infected at MOI-2×10⁶), as indicated by TUNEL staining (green). MYO7A (magenta) marks hair cells, SOX2 (red) marks supporting or progenitor cells, and DAPI (blue) labels nuclei. (B) Arginine supplementation (5 mM) reduces TUNEL-positive apoptotic cells in Cpd-silenced explants. (C) Quantification of apoptosis (% TUNEL-positive cells per total nuclei). Cpd silencing significantly increased apoptosis, which was partially rescued by arginine treatment. Data are presented as Mean \pm SEM from n = 4 explants per group from 2 different litters. No signal was artificially added or removed during the

quantification. **P < 0.001 by 1-way ANOVA with Tukey's multiple-comparison test. Scale bar: 100 μm .

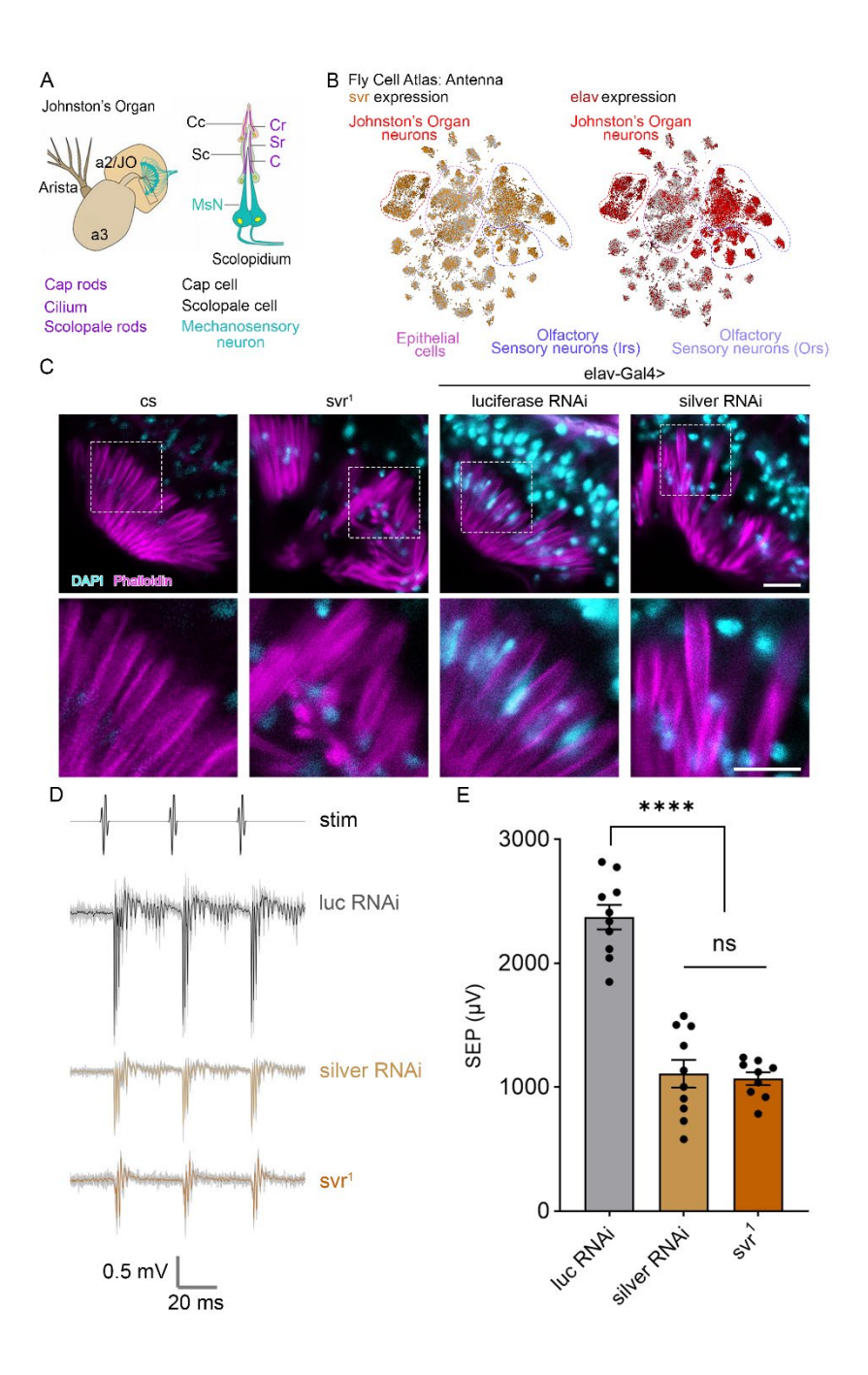


Figure 5: Loss of *silver* results in impaired morphology and function of Johnston's organ. **(A)** Schematic representation of *Drosophila* antenna. Mechanosensory neurons (labeled in cyan) are suspended within the JO, located in A2 segment. Schematic showing the organization of one scolopidium, including scolopale rods and actin bundles in the cilium, labeled in magenta (boxed area). Adapted from (28). **(B)** t-SNE plot showing *svr* (gold) and *elav* (red) expression in the

antenna using Scope: Fly cell atlas dataset (hongjie li 2022). (C) Confocal micrographs showing phalloidin labeling of scolopale rods, and actin bundles in the cilium (magenta), and nuclei labeled with DAPI (cyan) of cs or luciferase-RNAi control compared to svr^I and silver-RNAi. Boxed area highlights zoomed in region of disorganized actin bundles. Scale bar $10\mu m$. (D) Representative sound-evoked potential (SEP) traces recorded from antennae in response to presentation of simulated pulse song (stim). For each trace, the responses of 10 consecutive stimuli are shown in light grey, with the average of these 10 traces shown in the color representative of each genotype. (E) SEP amplitudes are plotted with each point representing a different antenna. Bars represent means, error bars represent SEM. ANOVA (p < 0.0001), Tukey's post hoc comparisons (**** p < 0.0001, ns = not significant).

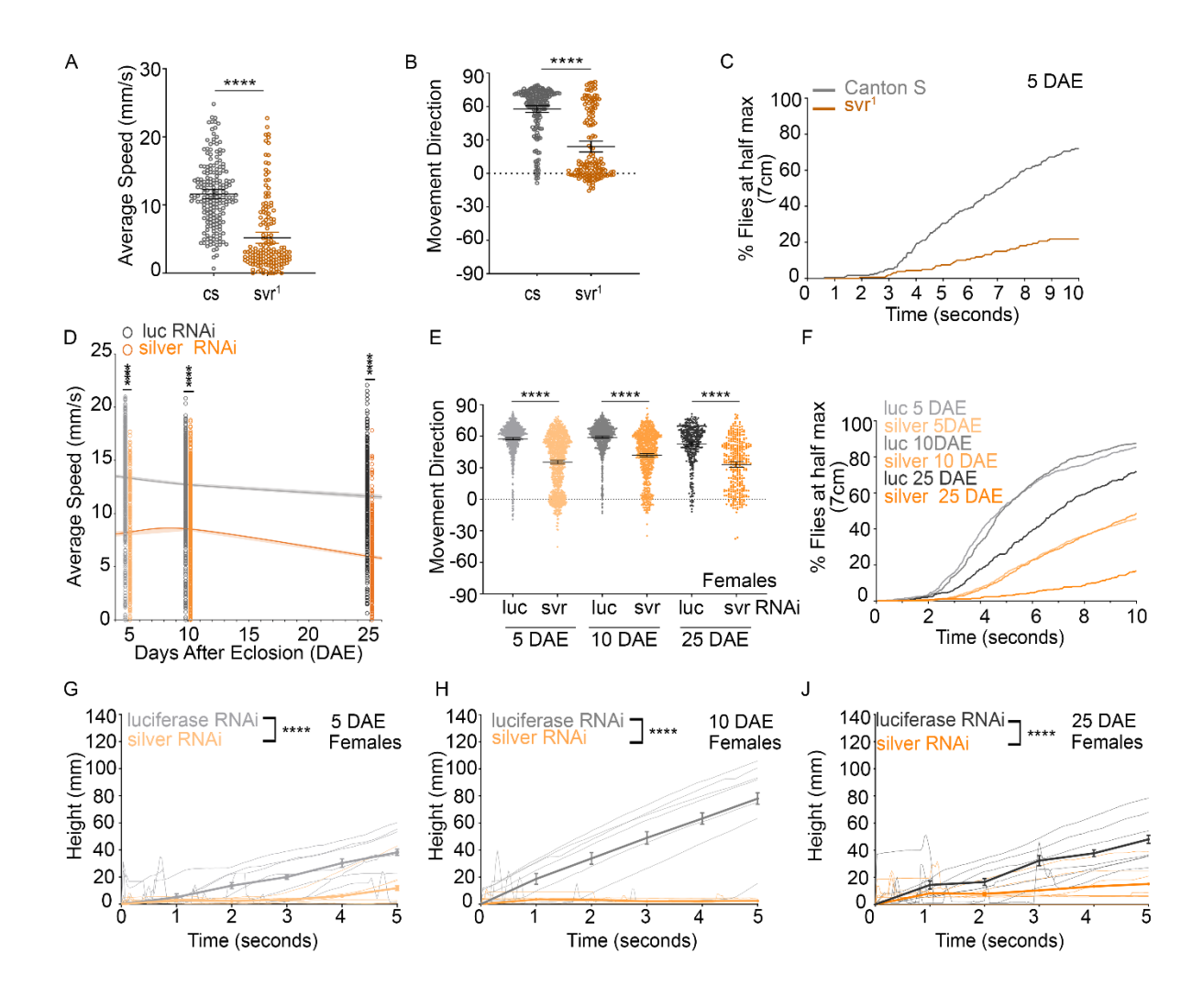


Figure 6: silver loss of function results in impaired negative geotaxis behavior. **(A-C)** Negative geotaxis analysis of canton-s (cs) (gray) control or svr^l (gold) in 5 DAE female flies. Assessment of average speed **(A)**, movement direction **(B)**, and percentage of flies that reached 7cm (half max) in 10 seconds for cs control (n = 190) or svr^l (n = 154) **(C)**. **(D-J)** Negative geotaxis analysis of pan-neuronal knockdown of luciferase control (gray) or silver (orange) in female flies. Assessment of average speed **(D)**, movement direction **(E)**, percentage of flies that reached 7cm in 10 seconds **(F)**, climbing distance at 5 DAE for luciferase control (n = 770) or silver (n = 1048) **(G)**, climbing distance at 10 DAE for luciferase control (n = 740) or silver (n = 775) **(H)**, and climbing distance

of 25 DAE for *luciferase* control (n = 350) or *silver* (n = 350) (**J**). Data are presented as mean + 95% CI. ****p<0.0001.

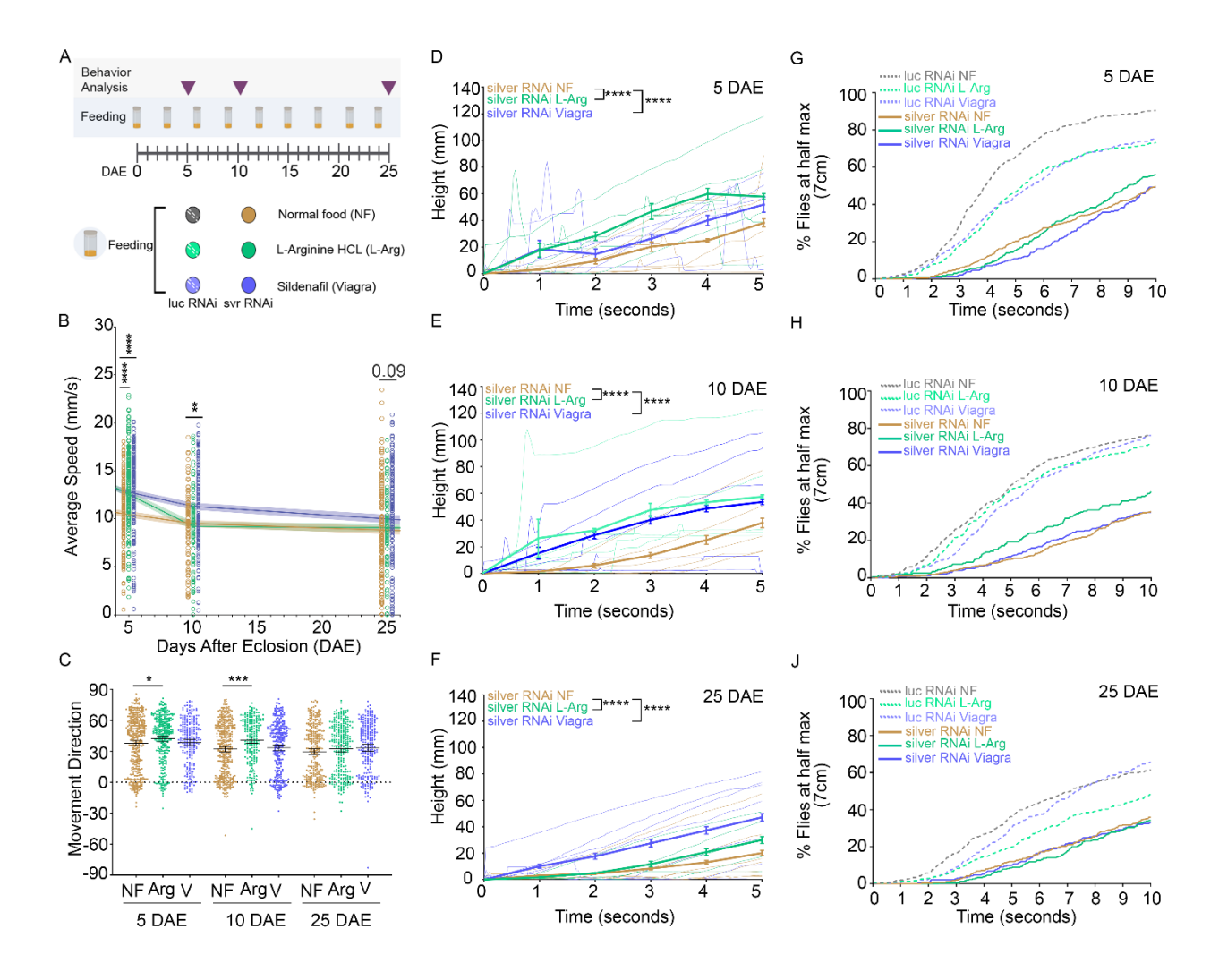


Figure 7: Feeding with L-Arginine or sildenafil improves negative geotaxis behavior in panneuronal *silver* knockdown flies. **(A)** Feeding paradigm for Normal food (NF), L-Arginine (L-Arg), and sildenafil (Viagra). **(B-F)** Negative geotaxis behavior for pan-neuronal knockdown of *silver* females (*elav*^{C155-GAL4}>*UAS- silver-RNAi*) fed with either NF (gold) (n = 140), L-Arg (green) (n = 180) or Viagra (blue) (n = 180). Assessment of average speed **(B)**, movement direction **(C)**, climbing distance at 5 DAE **(D)**, 10 DAE **(E)**, and 25 DAE **(F)** and percentage of *luciferase* (dashed lines) or *silver* (solid lines) flies to reach 7cm in 10 seconds for 5 DAE **(G)**, 10 DAE **(H)**

and 25 DAE (J). Data are presented as mean + 95% CI. ****p<0.05, **p<0.01, ***p<0.001, ****p<0.0001.